Volcanism in the Campania Plain:
Vesuvius, Campi Flegrei and Ignimbrites
edited by B. De Vivo

Chapter 7

Magmatic–hydrothermal fluid interaction and mineralization in alkali-syenite nodules from the Breccia Museo pyroclastic deposit, Naples, Italy

Luca Fedele[a,], Maurizio Tarzia[a], Harvey E. Belkin[b], Benedetto De Vivo[a], Annamaria Lima[a] and Jacob B. Lowenstern[c]*

[a]*Dipartimento di Scienze della Terra, Università degli Studi di Napoli, Federico II, Via Mezzocannone 8, Napoli 80134, Italy*
[b]*U.S. Geological Survey, 956 National Center, Reston, VA 20192, USA*
[c]*U.S. Geological Survey, Bldg 15, McKelvey Building, Menlo Park, CA 94025, USA*

Abstract

The Breccia Museo, a pyroclastic flow that crops out in the Campi Flegrei volcanic complex (Naples, Italy), contains alkali-syenite (trachyte) nodules with enrichment in Cl and incompatible elements (e.g., U, Zr, Th, and rare-earth elements). Zircon was dated at ~52 ka, by U–Th isotope systematics using a SHRIMP. Scanning electron microscope and electron microprobe analysis of the constituent phases have documented the mineralogical and textural evolution of the nodules of feldspar and mafic accumulations on the magma chamber margins. Detailed electron microprobe data are given for alkali and plagioclase feldspar, salite to ferrosalite clinopyroxene, pargasite, ferropargasite, magnesio-hastingsite hornblende amphibole, biotite mica, Cl-rich scapolite, and a member (probable davyne-type) of the cancrinite group. Detailed whole rock, major and minor element data are also presented for selected nodules. A wide variety of common and uncommon accessory minerals were identified such as zircon, baddeleyite, zirconolite, pollucite, sodalite, titanite, monazite, cheralite, apatite, titanomagnetite and its alteration products, scheelite, ferberite, uraninite/thorianite, uranpyrochlore, thorite, pyrite, chalcopyrite, and galena. Scanning electron microscope analysis of opened fluid inclusions identified halite, sylvite, anhydrite, tungstates, carbonates, silicates, sulfides, and phosphates; most are probably daughter minerals. Microthermometric determinations on secondary fluid inclusions hosted by alkali feldspar define a temperature regime dominated by hypersaline aqueous fluids. Fluid-inclusion temperature data and mineral-pair geothermometers for coexisting feldspars and hornblende and plagioclase were used to construct a pressure–temperature scenario for the development and evolution of the nodules. We have compared the environment of porphyry copper formation and the petrogenetic environment constructed for the studied nodules. The suite of ore minerals observed in the nodules supports a potential for mineralization, which is similar to that observed in the alkaline volcanic systems of southern Italy (Pantelleria, Pontine Archipelago, Mt. Somma-Vesuvius).

1. Introduction

Ore-forming fluids are either directly derived from magma or strongly influenced by the hydrothermal system attending the cooling magma body, or variable mixtures of the two. Recent studies have addressed the metallogenetic potential related to the extensive

*Corresponding author. *E-mail address*: lufedele@unina.it (L. Fedele).

alkaline volcanism of the Campanian Province, southern Italy. Paone (1999) and Paone et al. (2001) pointed out the similarity between the Mt. Somma-Vesuvius volcanic system and mineralized alkaline volcanic systems in general (e.g., Kelley et al., 1998). Detailed studies carried out by De Vivo et al. (1995) and Belkin et al. (1996) on cognate syenite nodules from the nearby islands of Ventotene and Ponza (Pontine Archipelago) have documented the existence of immiscibility between hydrosaline fluids and silicate melt, proving the presence of hydrothermal fluids of magmatic origin that are very similar to those reported from porphyry copper systems (Roedder, 1984; Cline and Bodnar, 1994). Occurrences of this type are also reported from other subvolcanic systems of southern Italy such as Pantelleria (De Vivo et al., 1992, 1993; Lowenstern, 1994), Mt. Somma-Vesuvius (Fulignati et al., 1997; Gilg et al., 2001), and Campi Flegrei (CF) (Tarzia et al., 1999, 2000).

The CF volcanic system is the largest alkaline volcanic complex in the Campanian Province where the last eruption occurred in 1538 AD and that created the small cone, Monte Nuovo. However, the CF system, according to Rosi et al. (1983, 1991), Fisher et al. (1993), and Orsi et al. (1996), is also the source of the eruption of the Campanian Ignimbrite, considered as a unique event at 37 ka. In contrast, according to De Vivo et al. (2001) and Rolandi et al. (2003), the Campanian Ignimbrite (CI) has an age of 39 ka with an estimated volume of about 180 km^3 (dry rock equivalent) and is only one of the different ignimbrite events that originated from fissures (see also Bellucci et al., this volume), active at various times and places in the Campania Plain in the period from 300 to 18 ka. Large volumes of magma have also been emplaced prior to eruption(s) and some magma fraction is currently cooling at depth, driving the abundant geothermal manifestations observed in the CF volcanic system.

The Breccia Museo (BM), in the CF system, is a volcanic breccia of complex origin which contains abundant fragments of juvenile lava, country rock, hydrothermally altered rock, and feldspar-dominated cumulate nodules (syenites) that we interpret to represent portions of a magma chamber margin. These alkali-syenite nodules illustrate the processes, mineralogy, and chemistry of the magma–host rock–hydrothermal system interaction and show the metallogenetic potential of the CF volcanic system. Here we emphasize our study of the trapped fluids and present a general discussion of the observed mineralogy. More detailed presentations of the feldspathoid and zirconium minerals are in preparation.

1.1. The Breccia Museo eruption (geologic setting)

The BM, named by Johnston-Lavis (1889), is a volcanic breccia which crops out in the southwest sector of the CF, a large and active volcanic field located west of Naples, Italy (Fig. 1). Lirer et al. (1991) dated charcoal from the BM by ^{14}C at ~21 ka and considered it unrelated to the 39 ka CI. Many authors (Di Girolamo et al., 1984; Perrotta, 1992; Perrotta and Scarpati, 1994) propose an origin by explosive activity from distinct monogenetic vents, while several other studies (Rosi et al., 1983, 1991; Rosi and Sbrana, 1987; Rosi and Vezzoli, 1989) suggest that the BM is indeed associated with the CI and it is an unique event dated ~37 ka, originating from the CF caldera. Two recent comprehensive studies by De Vivo et al. (2001) and Rolandi et al. (2003) dated the CI at ~39 ka by $^{40}Ar/^{39}Ar$ from sanidine and suggested that the ignimbrite events originated from fissure emissions related to regional fault systems in the Campanian Plain.

Figure 1. Simplified map of a portion of the Campi Flegrei area showing the distribution of the Breccia Museo deposit (modified from Perrotta and Scarpati, 1994). The black circle indicates the inferred location of the eruption vent.

Perrotta and Scarpati (1994) divide the BM deposit into four stratigraphic units grouped into two overlapping depositional units: (1) Lower Depositional Unit (LDU), a poorly sorted, matrix-supported pyroclastic flow deposit; (2) Upper Depositional Unit, consisting of layers of lithic breccias, coarse welded spatter clasts, and pumice flow(s) [Breccia Unit (BU), Spatter Unit (SU), Upper Pumice Flow Unit (UPFU); Fig. 2]. Perrotta and Scarpati (1994) propose the formation of the BM by an unsteady density-stratified flow (e.g., Branney and Kokelaar, 1992) controlled by morphology.

Melluso et al. (1995) classified the products of the BM, which range from trachyte to trachyphonolite and are characterized by an assemblage dominated by sanidine (Or_{88-63}) ± Na-plagioclase (An_{33-27}) ± biotite ± titanomagnetite ± apatite. Chemical variations

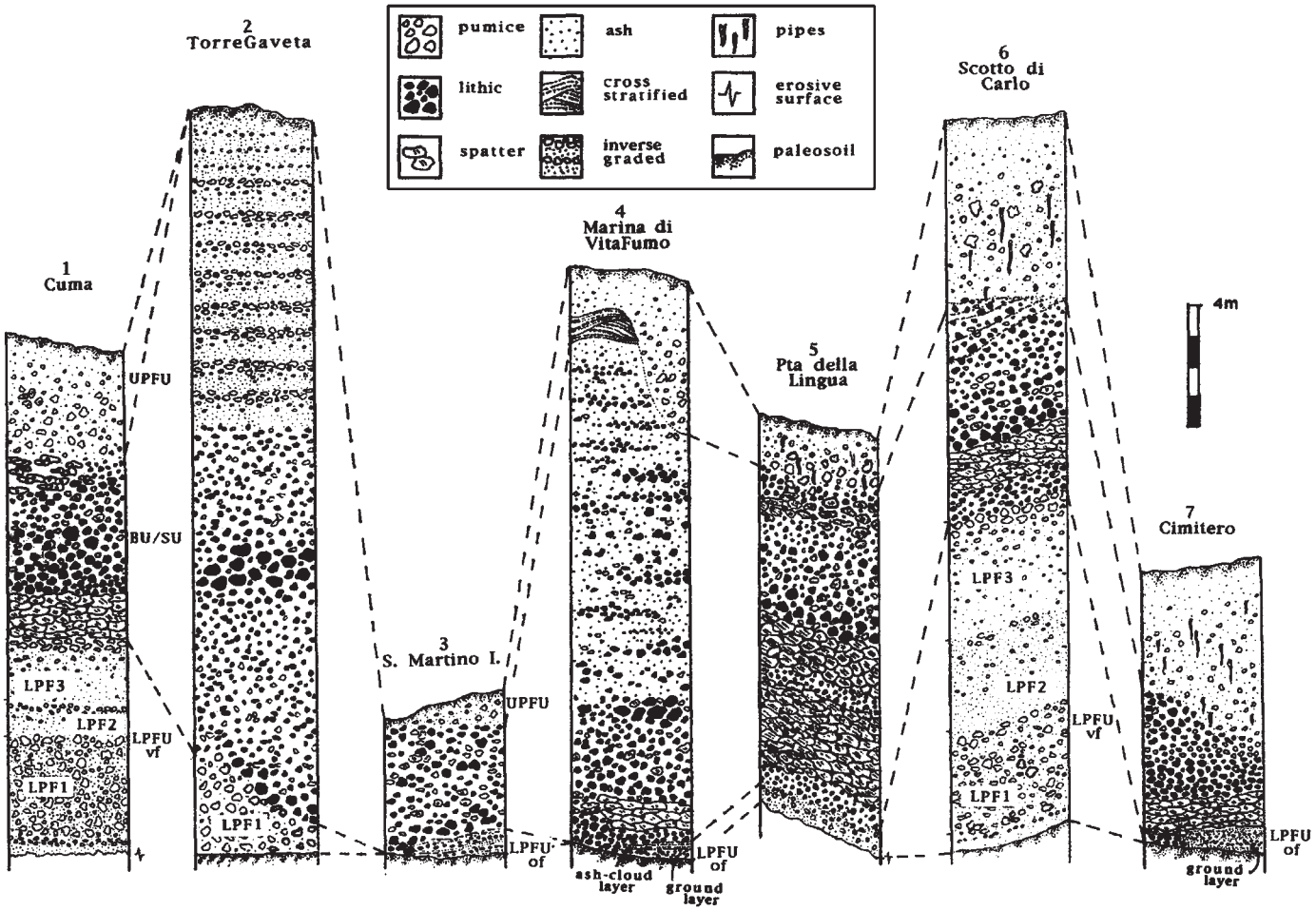

Figure 2. Stratigraphic sections of the BM member showing in detail the single units and their facies variations (after Perrotta and Scarpati, 1994). Locations are noted in Figure 1. LPFU, Lower Pumice Flow Unit; of, overbank facies; vf, valley facies. LPFU-associated layers are also indicated. BU (Breccia Unit) and SU (Spatter Unit) are grouped owing to the interfingering of the two units. For every unit, the maximum thickness is shown.

(major and trace elements) suggest an evolution from a less-differentiated trachyte by fractional crystallization of a sanidine-rich assemblage. Stratigraphic features and chemistry suggest the formation of the BM by progressive tapping of a thermally and chemically zoned shallow magma chamber.

1.2. Campi Flegrei hydrothermal system

De Vivo et al. (1989), carried out a detailed fluid inclusion (FIs) study on hydrothermal minerals from the CF geothermal system and identified an extensive alteration of the basement volcanic rocks and the existence of a shallow low-salinity fluid (~4% NaCl eq.) and deeper hypersaline fluids (>26% NaCl eq.) that were generated either by a continuous boiling process at depth, near a magmatic body, or by addition of magmatic fluids. Caprarelli et al. (1997) suggest the existence of two distinct reservoirs and origins for these geothermal fluids: (1) seawater infiltrated at relatively shallow depth (< 2000 m) and mixed with steam-heated groundwater, and (2) a deeper (>2000 m) hypersaline fluid of probable magmatic origin mixed with meteoric water. The two reservoirs show little mixing (if any) probably due to fluid density contrast.

All the data strongly suggest a similarity between the aqueous fluids associated with the CF–BM magma chamber(s) and the mineralized brines related to porphyry-type systems (Roedder, 1984). In these systems, there is increasing evidence that metal transport occurs in high-salinity brines or in hydrosaline melts which exsolved from silicate magmas (Roedder, 1971; Kilinc and Burnham, 1972; Cline and Bodnar, 1991, 1994; Kamenetsky et al., 1999).

The hydrothermal system of the BM (CF) magma chamber margin resembles the characteristics of other hydrothermal systems associated with the Italian alkaline volcanism, such as Pantelleria, Pontine islands, and Mt. Somma-Vesuvius (De Vivo et al., 1989, 1992, 1993, 1995; Lowenstern, 1994; Belkin et al., 1996; De Vivo, 1999; Paone, 1999; Gilg et al., 2001; Paone et al., 2001).

2. Studied samples

The nodules, generally light-colored, medium-grained, and ranging in size from 1 to 15 cm, were collected from the lithic horizon (BU) of the BM formation (Figs. 1 and 2). Sample MT14 was collected from Torre Franco-Verdolino (Soccavo); samples BL2, BL3, CFNA, VFB, BL8, MT17, MT19, MT20, MT21, MT22, MT24, and MT26 from Punta della Lingua (Procida), and sample MT27 from Scoglio cannone (Procida). Polished thin sections were prepared for microbeam analysis, crystals were separated for FI study, and a representative split of five selected samples was crushed and powdered for chemical analysis.

2.1. Radiometric age

In order to evaluate the timing and genetic relationships between the studied nodules, the BM eruption, and the CF volcanic system, we dated one sample using U–Th isotopic systematics of single zircon crystals extracted by crushing and hand picking from nodule

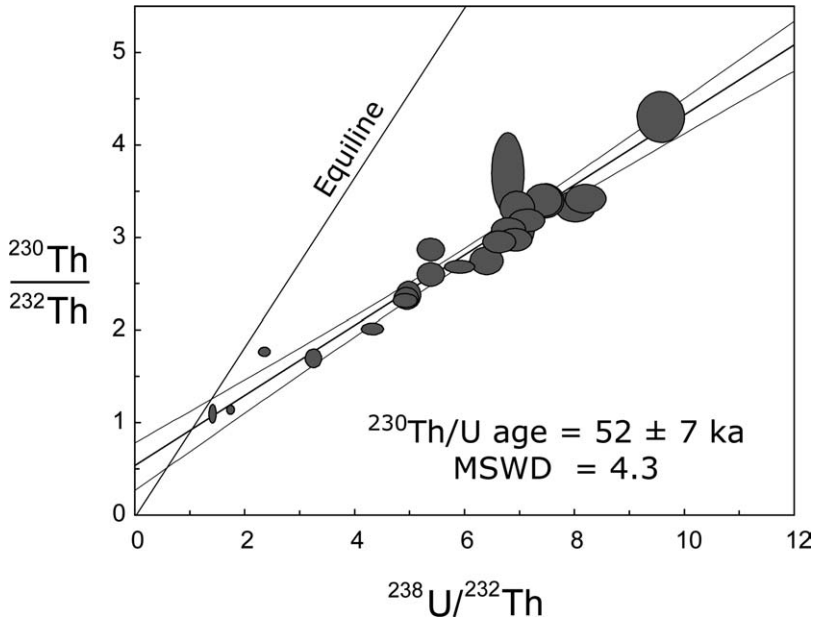

Figure 3. Plots of (^{238}U)/(^{232}Th) versus (^{230}Th)/(^{232}Th) for zircon crystals from a nodule (MT24) of the BM. The line through the data represents the least-squared regression (with MSWD) as calculated by ISOPLOT (Lowenstern et al., 2000). The age is calculated from the slope of the regression line. Data-point error ellipses represent 68.3% confidence.

MT24. Uranium and Th data were collected by one of us (Lowenstern) on the Stanford-USGS SHRIMP-RG SIMS, using analytical techniques and data reduction similar to those described in Lowenstern et al. (2000). Eighteen different zircons were analyzed (one of the 18 was analyzed seven times to check for data consistency). Analyses give model ages between 39 and ~100 ka, but the oldest and youngest two have much larger errors (Fig. 3). The oldest zircon has low U/Th and thus is more subject to errors as it is closer to the intercept. Owing to the fact that all the data fall very close to a straight line, we conclude that all the zircons were crystallized within a very narrow window of a few thousand years. However, some zircons could be older. The calculated model age is 52 ± 7 ka (Fig. 3), which is compatible with one of the proposed ages for the BM (≈37 ka, Rosi et al., 1983, 1991; Rosi and Sbrana, 1987; Rosi and Vezzoli, 1989).

2.2. Analytical methods

FI measurements were carried out on a Linkam THS600 heating–freezing stage at the Dipartimento di Scienze della Terra, Università degli Studi di Napoli, Federico II. The stage was calibrated for the temperature range of interest using synthetic FIs. Precision can be estimated at ±1°C in the range 200–350°C.

The nodules were studied at the U.S. Geological Survey, Reston, VA, USA using a JEOL-840 scanning electron microscope (SEM) equipped with a Princeton Gamma-Tech

energy-dispersive X-ray fluorescence analyzer (SEM-EDS) and a JEOL JXA-8900 fully automated, five-spectrometer electron microprobe for wavelength-dispersive analysis (EMPA). Electron microprobe operating conditions were 20 kV voltage and 30 nA beam current for oxides and sulfides and 15 kV voltage and 20 nA beam current for other phases. Reported beam currents were measured with a Faraday cup. Minor elements were counted for 60 s and major elements for 20 s. Standardization was done before each analytical session on synthetic and natural silicates, oxides, glasses, and phosphates. Count data were reduced online by a ZAF or phi-rho-z correction algorithm as supplied by JEOL USA, Inc. Analytical chemistry was done by Activation Laboratories, Ancaster, Ontario, Canada. Inductively coupled plasma mass spectrometry (ICP-MS) and inductively coupled plasma-atomic emission spectrometry (ICP-AES) were done on solutions using a lithium metaborate/tetraborate fusion procedure before sample dissolution with multiple acids. Other analytical techniques were: loss on ignition (LOI) by gravimetric (GRAV) techniques, infrared spectrometry (INFR), ion selective electrode (ISE), prompt gamma neutron activation analysis (PGNAA), and instrumental neutron activation analysis (INAA).

2.3. Chemistry of the samples

Table 1 gives the detailed chemical data for major, trace, and volatile elements in five representative samples. The nodules, medium-grained alkali-feldspar accumulations, compositionally are classified as syenites (trachyte equivalents) (Le Maitre, 2002). Samples containing scapolite and cancrinite-group minerals have a noticeable enrichment in Cl. Table 2 compares the mean of our five analyses of the BM nodules with the CI. The data show a strong chemical similarity supporting our assumption that the studied nodules are cognate and represent a medium-grained equivalent of the common products erupted from the CF volcanic system. Figure 4A shows the range of compositions on the total alkali-silica diagram (Le Maitre, 2002). The compositional range reflects the observed mineralogy. Figure 4B shows the co-variation of K_2O with CaO, Na_2O, and FeO (total). The good correlation (CaO, $r^2 = 0.82$; Na_2O, $r^2 = 0.43$; FeO, $r^2 = 0.96$) illustrates that the compositions result from a two-component mixture of A – magmatic alkali feldspar with oxides and mafics and B – late-stage Na-rich plagioclase, scapolite, and cancrinite-group minerals. The details of the mineralogy (see below) are different from typical CI or other CF rock compositions, which reflects their different formation histories; the nodules have been affected by pervasive late-stage magmatic fluids. Some nodules show high values of certain elements, for example, Zr in sample MT26 or Zn in sample BL2 (Table 1). This reflects the fact that each nodule represents a unique sample of the magma chamber margin where different volumes have been affected by somewhat different conditions with regard to incompatible elements and volatiles. The similarity in SiO_2, Al_2O_3, and total alkalis plus CaO confirm that the nodules are essentially accumulations of alkali feldspar with minor plagioclase and mafic minerals.

2.4. Petrography and mineralogy of the samples

The syenite nodules are primarily composed of potassium feldspars (up to ~80%) with subordinate plagioclase, scapolite, a S- and Cl-rich member of the cancrinite group, amphibole, pyroxene, biotite, magnetite, titanite, apatite, and uncommon sodalite. SEM-EDS and

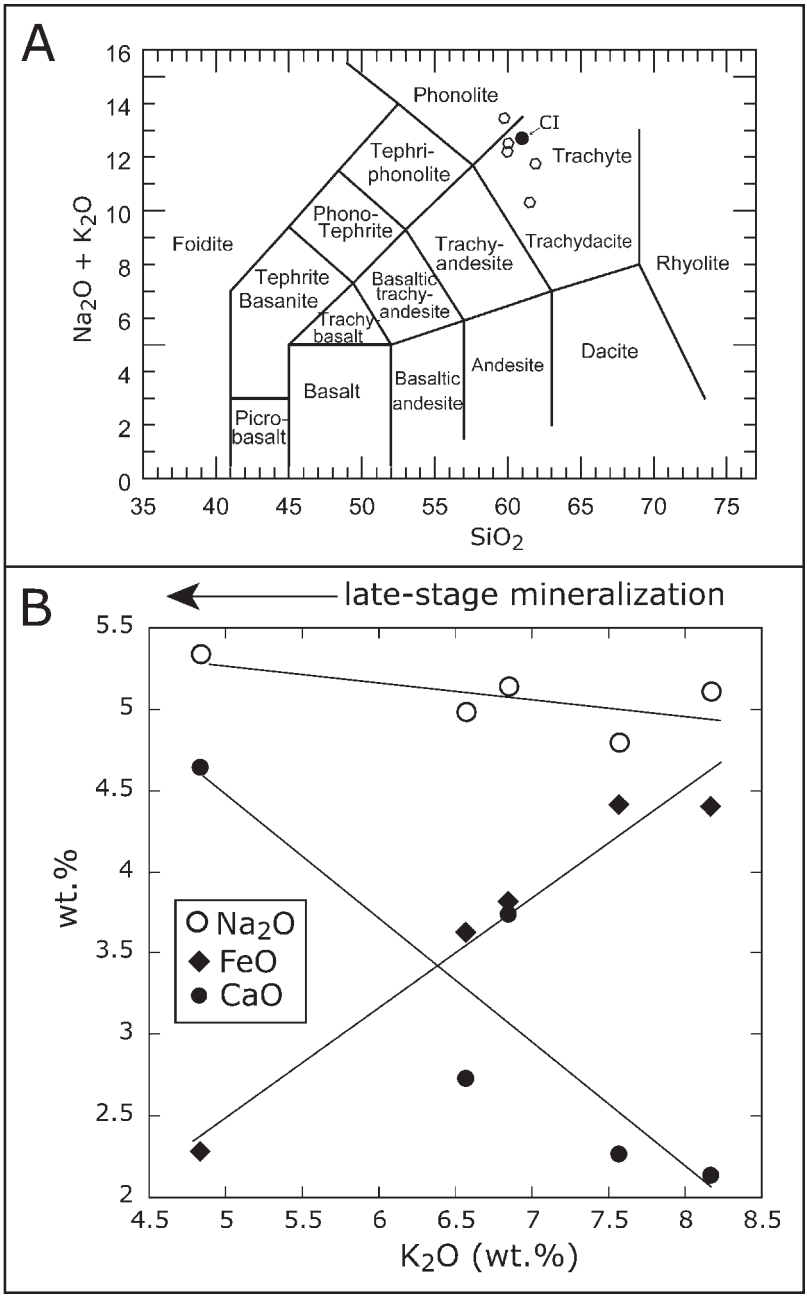

Figure 4. (A) Plot of nodule whole-rock chemistry on the total alkali versus silica (TAS) diagram of Le Maitre (2002). The five nodules are shown as open symbols and the average of 40 CI pumices (H.E. Belkin, unpublished data) also is shown as the black filled circle (CI). (B) Co-variation of selected chemistry of the five analyzed nodules. The linear regression curves for ◆K_2O–FeO, r^2=0.96; OK_2O–Na_2O, r^2=0.43; and ●K_2O–CaO, r^2=0.82 are shown. The nodule compositions can be modeled as a two-component mixture of magmatic alkali feldspar, oxides, and mafics affected by late-stage mineralization (arrow), which contains less FeO, more CaO, and slightly more Na_2O.

Table 1. Chemical analyses of BM nodules. The following elements were analyzed but were below the detection limit; element (detection limit): CO_2 (0.05%), Ag (0.5 ppm), In (0.1 ppm). The particular method of analysis is given in the right column (definitions in text).

Sample	BL2 (%)	BL8 (%)	MT14 (%)	MT19 (%)	MT26 (%)	Method
SiO_2	59.19	60.98	61.10	59.16	59.54	ICP-AES
TiO_2	0.44	0.62	0.42	0.44	0.44	ICP-AES
Al_2O_3	18.71	19.47	18.04	18.59	19.30	ICP-AES
FeO*	4.40	2.28	3.63	3.82	4.41	ICP-AES
MnO	0.29	0.10	0.19	0.06	0.18	ICP-AES
MgO	0.45	0.82	0.86	0.51	0.52	ICP-AES
CaO	2.14	4.64	2.73	3.75	2.27	ICP-AES
Na_2O	5.11	5.34	4.99	5.15	4.80	ICP-AES
K_2O	8.17	4.83	6.57	6.85	7.57	ICP-AES
P_2O_5	0.10	0.02	0.11	0.21	0.09	ICP-AES
F	0.19	0.08	0.20	0.07	0.30	ISE
Cl	1.10	0.05	0.08	1.64	0.25	INAA
SO_3**	0.10	0.02	<0.01	0.05	0.02	INFR
LOI	1.17	<0.01	0.61	1.11	0.58	GRAV
−O=F,Cl	0.33	0.04	0.10	0.40	0.18	
Total	101.23	99.21	99.42	101.01	100.09	
ppm						
As	11	<5	9	10	27	ICP-MS
B	30	16	39	13	29	PGNAA
Ba	16	143	339	235	30	ICP-AES
Be	13	17	11	19	14	ICP-AES
Bi	0.31	<0.06	0.16	0.14	0.23	ICP-MS
Ce	198	176	182	217	230	ICP-MS
Co	2	<1	4	5	3	ICP-MS
Cr	<20	<20	<20	30	36	ICP-MS
Cs	25.5	1.7	37.3	10.4	103	ICP-MS
Cu	<10	12	<10	68	20	ICP-MS
Dy	8.73	8.75	7.86	10.4	10.1	ICP-MS
Er	5.38	4.86	4.43	5.80	6.16	ICP-MS
Eu	1.92	2.46	1.76	2.63	2.01	ICP-MS
Ga	22	23	21	22	24	ICP-MS
Gd	9.36	10.5	9.20	13.1	10.8	ICP-MS
Ge	1.5	1.3	1.4	1.3	1.4	ICP-MS
Hf	13.0	7.0	10.4	11.3	14.3	ICP-MS
Ho	1.74	1.67	1.47	1.95	1.94	ICP-MS
La	107	72.2	98.1	95.5	122	ICP-MS
Lu	0.863	0.641	0.660	0.780	1.04	ICP-MS
Mo	11	2	4	4	6	ICP-MS
Nb	90.3	94.4	72.8	100	109	ICP-MS
Nd	67.7	74.6	63.7	89.3	79.2	ICP-MS
Ni	<15	16	<15	44	46	ICP-MS
Pb	59	8	26	24	32	ICP-MS
Pr	20.3	21.0	18.9	25.3	23.8	ICP-MS

Table 1. Continued

Sample	BL2 (%)	BL8 (%)	MT14 (%)	MT19 (%)	MT26 (%)	Method
Rb	499	183	255	301	379	ICP-MS
Sb	0.9	<0.2	1.4	0.3	1.6	ICP-MS
Sc	2	3	4	2	2	ICP-AES
Sm	11.5	12.6	10.8	15.2	13.2	ICP-MS
Sn	7	11	4	11	8	ICP-MS
Sr	40	329	233	310	102	ICP-AES
Ta	5.2	5.0	4.4	5.5	6.3	ICP-MS
Tb	1.59	1.60	1.42	2.01	1.81	ICP-MS
Th	40.2	20.0	37.0	34.7	48.0	ICP-MS
Tl	2.25	0.44	0.52	0.70	3.83	ICP-MS
Tm	0.829	0.689	0.670	0.833	0.970	ICP-MS
U	17.5	2.89	12.8	6.98	16.2	ICP-MS
V	29	22	41	32	34	ICP-AES
W	21	1.9	5.5	3.2	2.8	ICP-MS
Y	56	52	46	61	63	ICP-AES
Yb	5.36	4.27	4.18	5.04	6.49	ICP-MS
Zn	112	<30	69	<30	53	ICP-MS
Zr	658	285	487	539	735	ICP-AES

FeO*, total iron; SO_3**, total sulfur.

Note: Less than values equal not detected at the lower limit.

electron microprobe analysis of these nodules has identified U- and Zr-bearing phases such as uranpyrochlore, U-bearing thorite, U-and REE-bearing phosphate (monazite group), U-bearing zircon, baddeleyite and probable zirconolite and, less abundant, sulfides, carbonates, and tungstates.

The interlocking nature of the feldspar crystals gave rise to small angular cavities/vugs. No glass was identified in these cavities (except in one sample, VFB) suggesting that the phases found therein precipitated from a dense, supercritical aqueous fluid. Thus, the nodules are a mix of major phases precipitated from a silicate liquid and minor phases precipitated from a late-stage aqueous fluid permeating and moving through a volume of earlier-formed crystals.

3. Nodules: mineral chemistry and petrography

Feldspars. Sanidine is by far the most abundant phase (Fig. 7A,B) with an approximate composition of $Or_{73}Ab_{26}An_1$, whereas early plagioclase has a typical composition of $Or_5Ab_{55}An_{35}$ (Table 3). The sanidine composition is fairly homogeneous from core to rim, suggesting equilibrium with the host liquid; neither Sr nor Ba were detected by EMPA. Early-formed plagioclase, characterized by euhedral to subhedral crystal shapes, is more calcic than late-stage plagioclase (Fig. 5A,B). Late-stage plagioclase is found in and around crystals of scapolite and cancrinite group minerals (Fig. 7E). The feldspars contain aqueous FIs and melt inclusions (see below). Crystallization temperatures were estimated with the two-feldspar geothermometer, using the software SOLVCALC (Wen and

Table 2. Comparison between the mean chemical analysis of five selected BM nodules and the CI. Also shown is the maximum value.

	Nodules (%) (n = 5)	Campanian Ignimbrite[a] (%) (n = 40)
SiO_2	59.99	59.70
TiO_2	0.47	0.44
Al_2O_3	18.82	18.53
FeOT	3.71	3.32
MnO	0.16	0.18
MgO	0.63	0.70
CaO	3.11	2.43
Na_2O	5.08	4.75
K_2O	6.80	7.66
P_2O_5	0.11	0.14
F	0.17	0.16
Cl	0.62	0.40
S	0.02	0.01
LOI	0.69	1.09
Selected trace elements Maximun values = (x)		
ppm		
Ba	170.1 (339)	339.9
Ce	196.8 (230)	185.4
Cu	21.6 (68)	20.0
Eu	2.1 (2.63)	1.6
Hf	11.0 (14.3)	10.0
Lu	0.8 (1.04)	0.6
Nb	90.1 (109)	77.3
Pb	45.0 (59)	47.0
Rb	312.3 (499)	347.0
Sm	12.3 (15.2)	11.9
Sr	210.3 (329)	234.3
Th	36.1 (48)	38.7
U	11.4 (17.5)	11.4
W	6.6 (21)	4.6
Y	54.3 (63)	52.0
Yb	4.9 (6.49)	4.3
Zn	58.9 (112)	100.5
Zr	537 (735)	484

[a]H.E. Belkin (unpublished data).

Nekvasil, 1994), and ranged from 650°C to 725°C for late-stage phases and from 810°C to 890°C for early-formed phases (see discussion below).

Pyroxene. The clinopyroxene, typically salite to ferrosalite (Table 4) is slightly pleochroic, subhedral to anhedral, and sometimes zoned (Fig. 7B). It also occurs as euhedral crystals in

Table 3. Representative EMPA analyses of alkali and plagioclase feldspars in the BM nodules.

Sample	MT17.A	MT17.F	MT17.I	MT21.B	MT21.G	MT19.E	MT19.G	MT24.G	MT24.C	MT24.K	VFB.A	VFB.H	CFNA.A	CFNA.D	BL3.E	BL3.K
n	3	3	3	3	3	2	2	3	3	3	3	3	3	3	3	3
Com-ment	1×2 mm subhedral	200 µm euhedral	200 µm intersertal	2 µm euhedral	300 µm euhedral	1×2 mm euhedral	50 µm in S/C	600 µm euhedral	100 µm in S/C	1 µm euhedral	1 µm euhedral	500 µm euhedral	1×3 mm euhedral	2×4 mm euhedral	600 µm euhedral	300 µm subhedral
SiO_2	64.83	57.60	58.80	64.70	58.44	64.93	60.61	65.54	60.23	65.48	64.83	59.62	65.22	58.99	65.19	59.77
TiO_2	0.02	0.04	0.02	0.04	0.04	0.08	0.01	0.02	0.00	0.04	0.05	0.02	0.05	0.03	0.03	0.03
Al_2O_3	18.92	25.90	25.36	18.82	25.42	19.01	23.84	18.95	25.20	18.90	19.15	24.84	19.32	25.36	18.92	25.08
FeO	0.09	0.25	0.35	0.10	0.35	0.10	0.27	0.12	0.30	0.09	0.15	0.26	0.18	0.35	0.08	0.28
MgO	0.00	0.01	0.01	0.01	0.01	0.00	0.01	0.00	0.00	0.00	0.01	0.01	0.00	0.00	0.01	0.00
CaO	0.25	7.78	7.17	0.22	7.21	0.17	5.15	0.27	6.48	0.21	0.45	6.26	0.55	6.87	0.21	6.78
BaO	0.00	0.00	0.00	0.00	0.00	0.00	0.00	0.02	0.00	0.00	0.00	0.00	0.01	0.00	0.00	0.00
SrO	0.01	0.03	0.02	0.03	0.03	0.03	0.05	0.03	0.09	0.02	0.02	0.02	0.02	0.02	0.01	0.01
Na_2O	2.68	6.74	7.04	2.60	6.94	2.87	7.48	3.05	7.01	2.92	3.76	6.97	3.86	6.69	2.66	7.23
K_2O	12.40	0.44	0.49	12.85	0.59	12.29	1.09	12.06	0.60	12.30	10.78	1.18	10.63	1.13	12.86	0.60
P_2O_5	0.01	0.00	0.01	0.00	0.01	0.01	0.01	0.00	0.01	0.01	0.01	0.01	0.01	0.01	0.00	0.01
Sum	99.21	98.78	99.28	99.37	99.04	99.49	98.51	100.06	99.92	99.96	99.20	99.19	99.86	99.46	99.97	99.79

Number of ions on the basis of 32 (O)																
Si	11.920	10.441	10.584	11.910	10.554	11.904	10.944	11.935	10.733	11.942	11.867	10.732	11.855	10.611	11.920	10.688
Ti	0.003	0.005	0.003	0.006	0.006	0.011	0.001	0.002	0.000	0.005	0.006	0.003	0.007	0.004	0.004	0.004
Al	4.099	5.533	5.381	4.083	5.410	4.107	5.073	4.067	5.292	4.061	4.130	5.269	4.139	5.376	4.078	5.285
Fe^{3+}	0.014	0.037	0.053	0.015	0.053	0.016	0.041	0.018	0.045	0.014	0.023	0.040	0.028	0.052	0.013	0.042
Mg	0.001	0.002	0.002	0.001	0.003	0.000	0.002	0.001	0.001	0.000	0.002	0.002	0.000	0.001	0.002	0.000
Ca	0.050	1.512	1.383	0.043	1.396	0.033	0.995	0.053	1.236	0.041	0.089	1.207	0.108	1.323	0.042	1.299
Ba	0.000	0.000	0.000	0.000	0.000	0.000	0.000	0.001	0.000	0.000	0.000	0.000	0.000	0.000	0.000	0.000
Sr	0.001	0.003	0.002	0.003	0.003	0.003	0.006	0.003	0.009	0.002	0.002	0.002	0.002	0.003	0.002	0.001
Na	0.954	2.369	2.457	0.928	2.430	1.018	2.617	1.076	2.422	1.032	1.334	2.432	1.359	2.334	0.942	2.508
K	2.908	0.102	0.112	3.018	0.136	2.874	0.252	2.802	0.136	2.861	2.516	0.272	2.465	0.260	2.999	0.137
P	0.001	0.001	0.001	0.001	0.001	0.001	0.001	0.001	0.001	0.001	0.001	0.001	0.002	0.001	0.001	0.001
Sum	19.951	20.003	19.979	20.008	19.990	19.967	19.931	19.958	19.876	19.959	19.972	19.961	19.964	19.965	20.000	19.965
An	1.3	38.0	35.0	1.1	35.2	0.8	25.8	1.3	32.6	1.0	2.3	30.9	2.7	33.8	1.1	32.9
Ab	24.4	59.5	62.2	23.3	61.3	25.9	67.7	27.4	63.8	26.2	33.9	62.2	34.6	59.6	23.6	63.6
Or	74.3	2.5	2.8	75.7	3.4	73.2	6.5	71.3	3.6	72.7	63.9	6.9	62.7	6.6	75.3	3.5

FeO*, total iron; in S/C, an inclusion in scapolite or a cancrinite group mineral; 0.00, below detection limit.

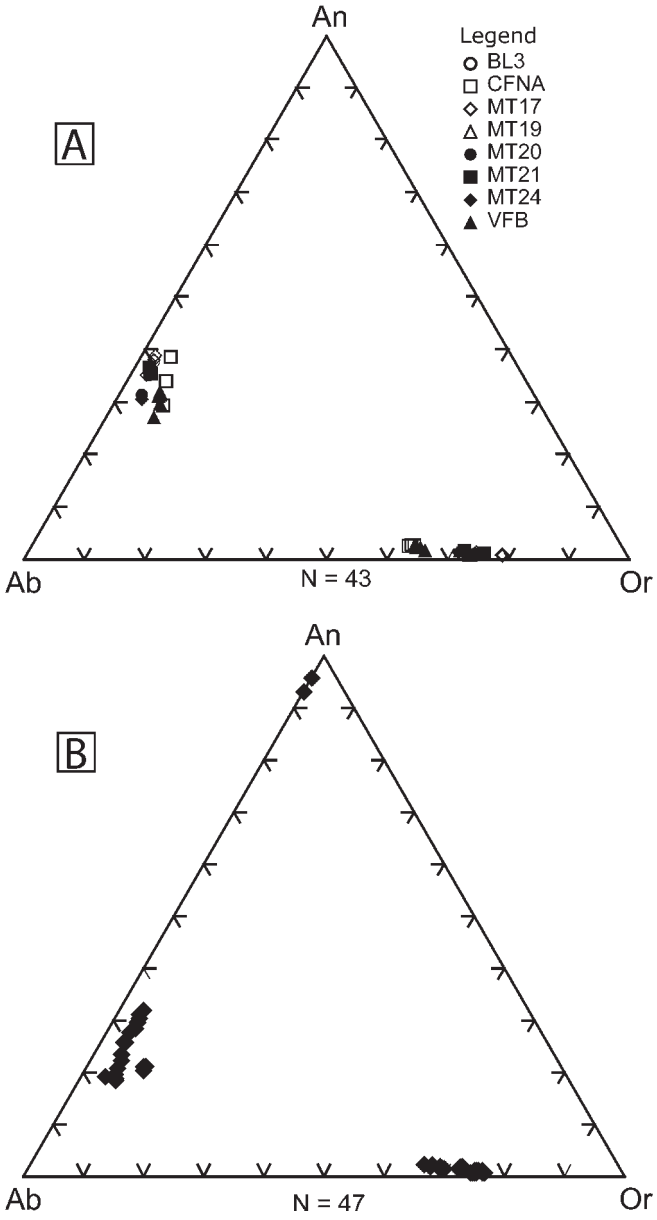

Figure 5. (A) Composition of early-stage alkali feldspar and plagioclase plotted on the mole % An–Ab–Or ternary diagram. (B) Composition of late-stage alkali feldspar and plagioclase plotted on the mole % An–Ab–Or ternary diagram. Legend applies to both diagrams. The two data points closest to the An apex in Figure 5B from sample MT24 are plagioclase crystals found in a mixture of scapolite and a cancrinite-group mineral.

Table 4. Representative EMPA analyses of clinopyroxenes in the BM nodules.

Sample	MT24.D	CFNA.F	MT17.D	MT20.E-rim	MT20.E-core	MT14.15	MT19.D
n	3	2	3	1	1	1	3
Comment	1 μm anhedral, zoned	100 μm subhedral	200 μm subhedral	1 μm subhedral, zoned	1 μm subhedral, zoned	200 μm subhedral	300 μm subhedral in vein
SiO_2	50.49	50.03	50.86	48.34	50.48	51.41	51.28
TiO_2	0.29	0.77	0.61	0.70	0.77	0.60	0.25
Al_2O_3	2.25	3.29	2.58	3.48	3.14	2.04	1.69
Cr_2O_3	0.01	0.00	0.01	0.01	0.00	0.00	0.01
FeO*	12.76	10.39	9.60	14.38	9.82	9.81	11.44
MgO	9.55	11.11	11.74	7.78	11.39	11.97	10.16
CaO	21.66	21.95	21.80	20.44	22.20	20.86	22.24
MnO	0.96	0.91	0.76	1.77	0.75	0.97	1.41
K_2O	0.00	0.00	0.00	0.00	0.02	0.05	0.00
Na_2O	0.69	0.71	0.54	1.17	0.63	0.69	0.76
Total	98.66	99.14	98.50	98.07	99.18	98.40	99.25
Formulae on the basis of 6 (O)							
Si	1.954	1.909	1.941	1.908	1.918	1.962	1.967
Al^{4+}	0.046	0.091	0.059	0.092	0.082	0.038	0.033
Al^{6+}	0.057	0.057	0.057	0.069	0.059	0.053	0.044
Fe^{3+}	0.035	0.064	0.013	0.106	0.039	0.006	0.046
Cr	0.000	0.000	0.000	0.000	0.000	0.000	0.000
Ti	0.008	0.022	0.017	0.021	0.022	0.017	0.007
Fe^{2+}	0.377	0.266	0.292	0.367	0.272	0.305	0.320
Mn	0.032	0.029	0.025	0.059	0.024	0.031	0.046
Mg	0.551	0.632	0.668	0.458	0.645	0.681	0.581
Ca	0.898	0.897	0.891	0.864	0.904	0.853	0.914
Na	0.052	0.053	0.040	0.090	0.046	0.051	0.057
K	0.000	0.000	0.000	0.000	0.001	0.002	0.000
Total	4.010	4.020	4.003	4.034	4.012	4.001	4.014
Mg	28.3	32.6	34.6	23.6	33.4	35.3	29.6
ΣFe**	22.8	18.5	17.1	27.4	17.3	17.8	20.9
Ca	46.2	46.2	46.2	44.5	46.8	44.2	46.6

FeO*, total iron; ΣFe** = (Fe^{2+} + Fe^{3+} + Mn).

Note: Fe^{2+}, Fe^{3+} calculated using the method of Droop (1987).

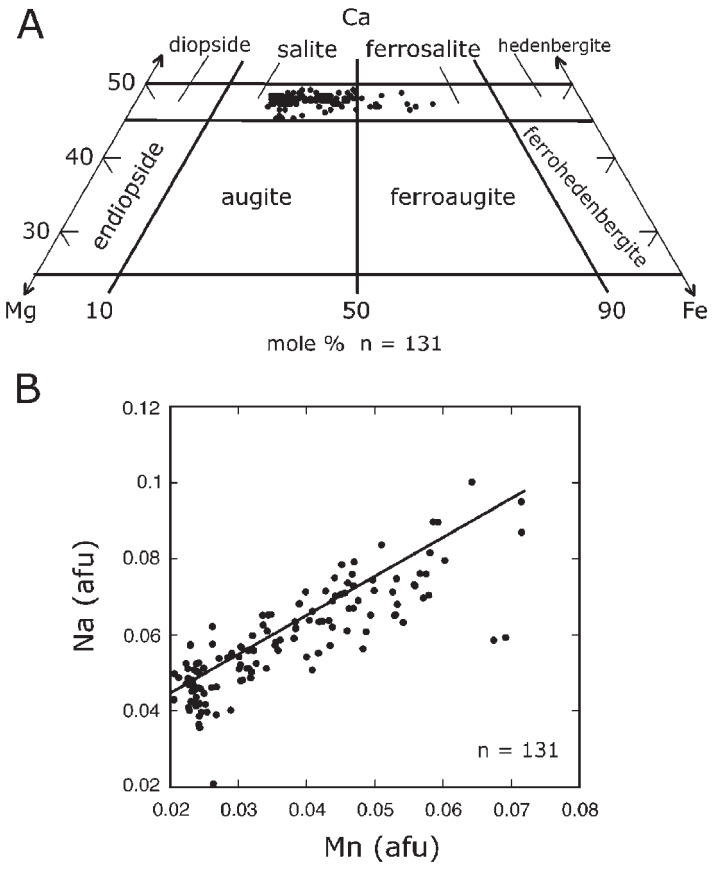

Figure 6. (A) A portion of the pyroxene quadrilateral showing the compositional range of the clinopyroxenes measured by EMPA in all the studied nodules. (B) Co-variation of Na and Mn (afu – atom formula unit) in the clinopyroxenes shown in the quadrilateral. The linear regression of the Na and Mn data is positive with $r^2 = 0.70$.

crosscutting veins or cavities/vugs. Pyroxene is often associated with amphibole, biotite, titanite, and Fe–Ti oxides. Figure 6A shows that these pyroxenes have essentially constant Ca but vary in Mg and Fe. Rims, visible in transmitted light and SEM analysis, typically are enriched in Fe, Na, and Mn (Table 4, sample MT20.E). Figure 6B shows the positive co-variation between Na and Mn. The acmite ($NaFe^{3+}Si_2O_6$) component in the studied clinopyroxenes varies from 1.1 to 5.5. Clinopyroxenes in the BM pyroclastics typically are somewhat more Mg-rich and range from diopside to ferrosalite (Melluso et al., 1995). The studied clinopyroxenes in the nodules, enriched in Mn and Na, probably represent later-stage magmatic crystallization instead of early-magmatic crystallization.

Amphibole. The amphibole is a hornblende that varies in composition from ferropargasite, pargasite, to magnesio-hastingsite/pargasite (Table 5). This phase occurs in large euhedral to subhedral crystals, is slightly to moderately pleochroic, and is commonly zoned (Fig. 7A). The amphibole has moderate F, variable TiO_2, and a low Cl content (Table 5).

Table 5. Representative EMPA analyses of amphiboles in the BM nodules.

Sample	MT24.F (fp)	VFB.C (p)	BL3.B (p)	MT17.B (p)	MT21.C (p)	MT21.F (p)	MT19.E (mh-p)	MT20.D (mh-p)
Comment	2 mm anhedral, zoned	600 μm suhedral	1 mm euhedral	1 mm euhedral	1 mm subhedral, zoned	4 mm euhedral	300 μm euhedral in vein	600 μm euhedral
n	3	3	3	3	3	3	3	3
SiO_2	39.43	40.19	42.85	40.19	41.72	40.57	41.38	41.39
TiO_2	1.81	2.04	0.86	2.60	0.77	2.72	1.50	0.78
Al_2O_3	11.62	11.27	10.02	11.50	10.55	11.40	10.97	10.04
Cr_2O_3	0.00	0.00	0.00	0.00	0.00	0.00	0.00	0.00
FeO*	18.22	16.44	15.10	17.03	15.90	15.85	15.74	16.00
MnO	1.56	1.70	1.22	0.96	1.37	0.86	1.28	1.17
MgO	9.12	9.92	11.74	9.72	11.62	10.51	11.31	11.81
CaO	11.02	10.58	11.65	11.34	11.40	11.58	11.26	11.08
Na_2O	2.32	2.43	2.51	2.37	2.50	2.39	2.43	2.27
K_2O	1.86	1.91	1.92	1.99	1.86	1.91	1.88	2.18
F	2.40	1.87	2.61	2.28	2.61	1.83	2.54	3.31
Cl	0.10	0.10	0.24	0.14	0.09	0.13	0.11	0.14
−O = F,Cl	1.03	0.81	1.15	0.99	1.12	0.80	1.09	1.43
Total	98.42	97.65	99.57	99.12	99.28	98.95	99.29	98.75
Formulae calculated assuming 13 cations excluding Ca, Na, and K								
Si	5.990	6.110	6.304	6.018	6.189	6.060	6.131	6.161
Ti	0.207	0.234	0.095	0.293	0.086	0.305	0.167	0.087
Al	2.081	2.020	1.737	2.029	1.845	2.007	1.916	1.762
Cr	0.000	0.000	0.000	0.000	0.000	0.000	0.000	0.000
Fe^{3+}	0.000	0.000	0.000	0.000	0.000	0.000	0.000	0.000
Fe^{2+}	2.315	2.090	1.858	2.133	1.972	1.979	1.950	1.991
Mn	0.201	0.219	0.152	0.121	0.173	0.109	0.160	0.147
Mg	2.065	2.247	2.576	2.170	2.569	2.340	2.499	2.622
Ca	1.793	1.723	1.836	1.819	1.812	1.853	1.787	1.767
Na	0.682	0.715	0.716	0.687	0.720	0.693	0.697	0.656
K	0.361	0.370	0.361	0.380	0.352	0.363	0.355	0.415
F	0.126	0.098	0.137	0.120	0.137	0.096	0.134	0.174
Cl	0.003	0.003	0.007	0.004	0.003	0.004	0.003	0.004

fp, ferro-pargasite; p, pargasite; mh-p, magnesio-hastingsite/pargasite.

FeO* = total iron, Cr_2O_3=below detection limit.

Note: Fe^{3+} calculated using the method of Droop (1987).

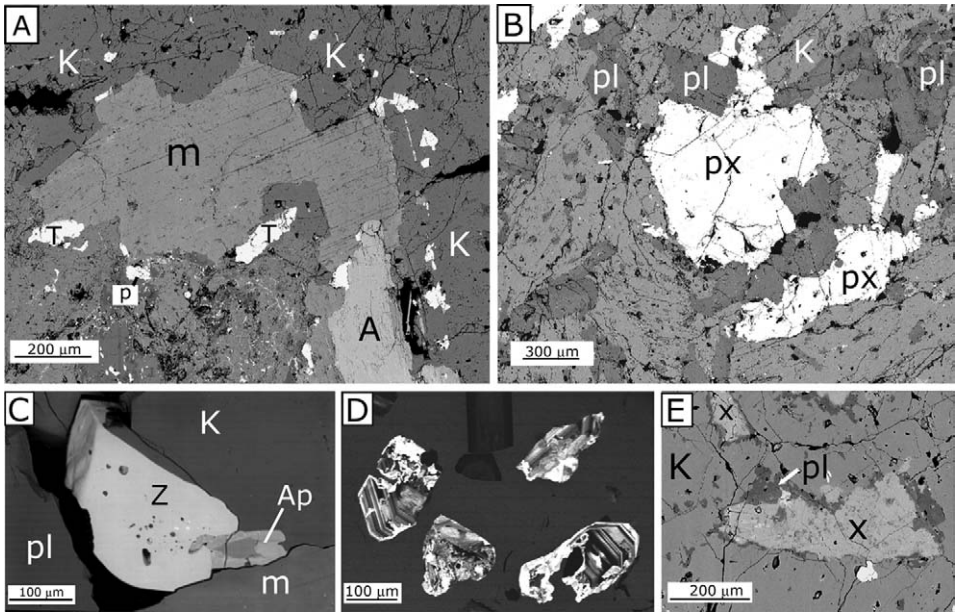

Figure 7. (A) SEM back-scattered image of sample MT21 showing late-stage biotite mica (m) and earlier amphibole (A) filling a vug formed by earlier crystallized alkali feldspars (K). Later phases, monazite (p) and titanite (T), enriched in incompatible elements, formed after the mafics. (B) SEM back-scattered image of sample MT20 showing clinopyroxene (px) and plagioclase (pl) forming with alkali feldspar (K). (C) SEM back-scattered image of sample CFNA illustrating the texture of late-stage zircon (Z) forming in a vug of alkali feldspar (K), plagioclase (pl), and biotite mica (m). The zircon has formed subsequent to the zoned apatite (Ap). (D) Cathodoluminescence image of hand-picked zircons used for U–Th age dating illustrating their complex zoning. (E) SEM back-scattered image of sample BL3 showing late-stage formation of scapolite plus a cancrinite-group mineral (X) in a vug formed by earlier alkali feldspar (K). Late-stage plagioclase (pl) appears to have formed just prior to the scapolite and cancrinite-group mineral.

Biotite. This phase was observed in only about half of the studied nodules. Typically, it fills open spaces formed by feldspar accumulations (Fig. 7A). Some are very F-rich (about 5–6 wt.%) but they are all low in Cl (less than 0.1 wt.%) and Ba (Table 6). We observed two compositional groups, one with higher TiO_2, F, and MgO and the other with lower TiO_2, F, and higher FeO.

Scapolite. Scapolite occurs in large crystals or inter-grown with cancrinite-group minerals (Fig. 7E) and contains FIs as well as vugs. Scapolite crystals are often associated with cancrinite-group minerals, titanite, apatite and Zr-bearing minerals, or subordinately, with amphibole, pyroxene, mica, and Fe–Ti oxides. The scapolite is marialitic (Table 7), the percentage of Me varies from 17 to 22, and is relatively enriched in K_2O. It is one of the two observed phases rich in Cl and from the textural relations, it is a later-stage phase in the nodules paragenesis.

Cancrinite-group minerals. The presence of these phases accounts for the enrichment of sulfur in the bulk composition of some of the analyzed samples (Table 1). This phase is also enriched in Cl and Na (Table 7). On the basis of the microprobe data (Table 7), these minerals are interpreted as members of the davyne-type cancrinite; most close to microsommite

Table 6. Representative EMPA analyses of biotite micas in the BM nodules.

Sample	CFNA.B (wt%)	CFNA.D (wt%)	CFNA.E (wt%)	MT21.A (wt%)	MT21.D (wt%)	MT21.E (wt%)
n	3	3	3	3	3	3
Comment	1 mm	200 µm	600 µm	600 µm	900 µm	1 mm
SiO_2	37.61	37.20	37.91	40.35	41.85	40.66
TiO_2	3.44	3.67	3.44	1.66	0.74	1.82
Al_2O_3	13.65	14.18	13.78	12.15	11.35	11.82
Cr_2O_3	0.00	0.00	0.00	0.00	0.00	0.00
FeO	13.41	13.90	13.49	10.80	9.47	10.39
MnO	0.93	0.95	0.95	0.65	0.65	0.63
MgO	16.32	15.69	16.34	19.27	20.69	19.60
CaO	0.02	0.01	0.01	0.01	0.00	0.01
BaO	0.03	0.02	0.00	0.00	0.00	0.03
Na_2O	0.58	0.63	0.64	0.32	0.32	0.42
K_2O	9.35	9.38	9.52	10.05	10.25	10.08
F	3.55	3.39	3.71	5.70	6.76	6.19
Cl	0.04	0.04	0.05	0.05	0.05	0.05
$-O = F,Cl$	1.51	1.44	1.57	2.41	2.85	2.62
H_2O calc	2.32	2.40	2.28	1.37	0.90	1.15
Sum	99.76	100.01	100.54	99.96	100.17	100.25
Formulae on the basis of 11 (O)						
Si	2.806	2.776	2.808	2.964	3.048	2.976
Al^{4+}	1.201	1.247	1.203	1.052	0.974	1.020
SumT	4.000	4.000	4.000	4.000	4.000	3.996
Al^{6+}	0.007	0.023	0.011	0.017	0.022	0.000
Ti	0.193	0.206	0.192	0.092	0.041	0.100
Cr	0.000	0.000	0.000	0.000	0.000	0.000
Fe	0.837	0.867	0.835	0.664	0.577	0.636
Mn	0.059	0.060	0.059	0.041	0.040	0.039
Mg	1.815	1.745	1.805	2.110	2.246	2.139
Sum*R*	2.911	2.901	2.902	2.923	2.926	2.915
Ca	0.002	0.001	0.001	0.001	0.000	0.001
Ba	0.001	0.001	0.000	0.000	0.000	0.001
Na	0.084	0.091	0.092	0.045	0.046	0.060
K	0.890	0.893	0.899	0.942	0.952	0.941
Sum*A*	0.977	0.986	0.992	0.988	0.998	1.003
F	0.839	0.801	0.868	1.323	1.556	1.433
Cl	0.005	0.005	0.006	0.006	0.006	0.006
OH calc	1.156	1.194	1.126	0.671	0.438	0.561
Mg/(Mg + Fe* + Mn)	0.67	0.65	0.67	0.75	0.78	0.76

Table 7. Representative EMPA analyses of cancrinite-group minerals and scapolite in the BM nodules.

Sample	MT17.B (C)	MT21.D (C)	BL3.G (C)	MT24.H (C)	Sample	MT24.D (S)	MT19.I (S)	MT20.G (S)
n	3	2	3	3	*n*	3	1	3
SiO_2	31.92	31.87	32.37	31.89	SiO_2	57.37	56.28	56.62
Al_2O_3	27.99	27.56	28.53	27.42	Al_2O_3	22.02	22.80	22.12
FeO*	0.04	0.08	0.08	0.09	FeO*	0.15	0.14	0.13
MgO	0.00	0.01	0.01	0.02	MgO	0.00	0.01	0.00
MnO	0.01	0.00	0.00	0.01	MnO	0.00	0.01	0.01
CaO	10.97	9.84	9.85	9.90	CaO	4.57	5.38	4.76
SrO	0.03	0.02	0.01	0.02	SrO	0.05	0.03	0.02
K_2O	4.02	3.64	3.59	2.82	K_2O	1.99	2.00	2.10
Na_2O	11.35	13.38	13.22	13.99	Na_2O	9.97	9.61	9.72
P_2O_5	0.02	0.01	0.02	0.01	P_2O_5	0.00	0.01	0.00
SO_3	1.22	3.56	3.32	4.81	SO_3	0.01	0.03	0.01
Cl	10.00	8.34	9.36	8.29	Cl	3.95	4.06	3.99
−O = Cl	2.26	1.88	2.12	1.87	CO_2**	0.17	0.02	0.09
Sum	95.30	96.41	98.25	97.40	−O = Cl	0.89	0.92	0.90
					Sum	99.37	99.46	98.66
Number of ions on the basis of 12 (Si, Al, Fe)					Number of ions on the basis of 12 (Si, Al)			
Si	5.899	5.939	5.883	5.957	Si	8.262	8.122	8.217
Al	6.098	6.054	6.111	6.036	Al	3.738	3.878	3.783
Fe	0.003	0.006	0.006	0.007	Fe	0.018	0.016	0.015
Mg	0.000	0.002	0.002	0.005	Mg	0.000	0.002	0.000
Mn	0.002	0.000	0.000	0.001	Mn	0.000	0.002	0.001
Ca	2.172	1.964	1.919	1.982	Ca	0.705	0.832	0.740
Sr	0.003	0.002	0.001	0.002	Sr	0.005	0.002	0.001
K	0.948	0.864	0.833	0.672	K	0.366	0.368	0.388
Na	4.069	4.833	4.659	5.066	Na	2.784	2.689	2.735
P	0.003	0.002	0.003	0.001	P	0.000	0.001	0.000
S	0.169	0.498	0.453	0.675	S	0.001	0.003	0.001
Cl	3.132	2.634	2.884	2.625	Cl	0.965	0.992	0.981
					Me%	18.7	21.8	19.5

C, cancrinite group; S, scapolite. FeO*, total iron; CO_2**, calculated by stoichiometry.

in composition (Ballirano et al., 1996; Deer et al., 2004). These cancrinite-group phases occur in late-stage masses, filling open spaces or vugs (Fig. 7E). The crystals are associated with Na-rich plagioclase and appear to be one of the last major silicate phases to be formed.

Titanite. This phase is common throughout the nodules (Fig. 7A). It occurs in a wide range of shapes, with subhedral to irregular habit and often shows moderate zonation. Some crystals are slightly enriched in REE and Zr. In growth around other crystals or filling cavities, titanite often is associated with Fe/Ti oxides and/or Zr-bearing minerals such as zircon and baddeleyite.

Apatite. Apatite occurs as small inclusions in feldspars, or in vugs as a late-stage mineral. It ranges in habit from anhedral masses to euhedral crystals of up to 100 μm in length.

Apatite sometimes is zoned and is frequently associated with zircon, monazite, and cheralite (Fig. 7C).

3.1. Uranium, REE, and zirconium-bearing minerals

The nodules have an exceptional assemblage of U (Table 8), REE, and zirconium-bearing minerals. The mineral habit and mode of occurrence strongly suggests deposition from dense, supercritical fluids, that separated from the crystallizing magma, and were enriched in incompatible elements. We have identified these phases by quantitative electron microprobe and SEM-EDS analysis. A separate paper in preparation will detail these phases.

Zircon typically is found associated with titanite, Fe–Ti oxides and, to a lesser extent, pyroxene, amphibole, and mica. Large crystals are zoned (Fig. 7D) and frequently host small uraninite/thorianite crystals. On the basis of petrography, we distinguish, two types of zircon. One type occurs as euhedral to subhedral grains and appears to have crystallized under magmatic conditions (Fig. 7D), whereas the other type fills cavities, is irregularly shaped, and appears to be hydrothermal in origin (Fig. 7C). The first type was separated from sample MT24 and was dated using the U–Th isotope method (see above).

Baddeleyite is found either in groups or isolated and shows a common bladed habit. Gianfagna (1985) reports baddeleyite from an ejected block from Colle Cimino, in the Alban Hills volcanic complex located just south of Rome, Italy. There, baddeleyite has a composition similar to that found in the BM nodules except for the lack of UO_2, and the host rock was also thought to represent a piece of magma chamber. Zircon and baddeleyite are enriched in UO_2 (Table 8), and baddeleyite is enriched in Nb_2O_5, up to 2.5 wt.%. The occurrence of both late-stage zircon and baddeleyite poses an interesting problem in mineral paragenesis, which we will not address in this presentation. However, we suggest that this is a worthy subject for further study, especially concerning the influence of F- and Cl-rich fluids on the relative stability of these two phases.

Zirconolite is a relatively rare accessory mineral, ideally $CaZrTi_2O_7$ in composition, but generally accommodating a large number of elements in its structure: in natural samples of zirconolite, 30 or more elements may be present at the 0.1–1.0 wt.% concentration level (Williams and Gieré, 1996). The main substitutions are: the REE and actinide elements for Ca; Hf for Zr; and Nb, Ta, Fe, Mn, Mg, and W for Ti. Zirconolite occurs in a wide range of rock types and paragenesis. The majority are from carbonatites (Gieré et al., 1998). Only four syenite occurrences have been reported out of a total of more than 50 terrestrial localities (Williams and Gieré, 1996): (1) at Glen Dessarry, Scotland (Fowler and Williams, 1986), (2) from the alkali intrusion of the Arbarastakh Massif, Russia (Borodin et al., 1960), (3) in syenite pegmatites in the Oslo region of Norway at Fredicksvärn (Brøgger, 1890) and Langesundfjord (Larsen, 1996), and (4) from a syenitic ejecta enclosed in a rock known as "sanidinite" found at Monte di Procida at Campi Flegrei, Italy (Mazzi and Munno, 1983). The analyses of the BM nodules show that some zirconolite crystals are enriched with thorium and uranium (Table 8) and have low to moderate REE content.

Pyrochlore, ideally $(Na,Ca)_2Nb_2O_6(OH,F)$, is a relatively common accessory phase in the nodules. This mineral shows a large compositional variation and is the main Nb-bearing mineral in the nodules, and some crystals that contain significant UO_2 are termed uranpyrochlore (Table 8).

Table 8. Uranium content of minerals in the studied nodules measured by EMPA.

Uranium content of minerals (given as wt.% UO_2 from EMPA data)	
Uraninite/thorianite	~29
Uranpyrochlore	~15
Thorite	~5
Zircon	0.1–2.0
Baddeleyite	0.06–1.2
Zirconolite	0.7–5.5
Monazite/cheralite	0.13–1.0
Apatite	dl–0.1
Titanite	dl–0.1

Detection limit (dl) = 0.05 wt.%.

Other phosphates. Monazite and cheralite also are common accessory minerals (Fig. 7A); often they show zoning and are typically enriched in ThO_2, light REE, and UO_2 (Table 8).

Other minerals. We observed a plethora of minor phases either identified by electron microprobe or SEM-EDS analyses; sulfides (pyrite, pyrrhotite; Pb-Cu-Fe- and Zn-sulfides), carbonates (calcite and cerussite), tungstates (scheelite and ferberite), and silicates (rare pollucite, sodalite, and celsian). Typically, these minerals occur in a variety of habits as single crystals commonly embedded in feldspar or associated with other phases growing in cavities. There are also common oxide phases ranging from magmatic titanomagnetite to various secondary Fe oxides resulting from subsequent alteration of earlier phases.

3.2. Fluid and melt inclusions

We used two approaches to study fluid and melt inclusions: (1) host crystals were fractured and a detailed SEM-EDS examination of these surfaces identified the wide variety of daughter crystals (or accidentally trapped crystals) observed with transmitted visible light and (2) microthermometric data were collected to constrain the conditions and composition of the trapped fluids. Fluid and melt inclusions in K-feldspar host crystals were examined. Thick sections (~300 μm thickness) were prepared for optical observation, whereas microthermometry was performed on K-feldspar crystals hand picked after crushing a selected subset of the available nodules. Inclusions that were found in healed fractures of the host minerals vary in shape and size but seldom exceed 30 mm in length.

Observations with transmitted light at room temperature revealed the presence of FIs containing numerous solids. The common occurrence of similar crystal habits, relative index of refraction, and phase proportions suggests that most are daughter minerals (i.e., precipitated from the trapped fluid during cooling). In order to identify these crystals, some small pieces of nodules were carefully fractured and the fresh surface was examined by SEM techniques.

Spectra collection and EDS analysis of the daughter minerals presented many difficulties owing to their small size and the random orientation of the analyzed samples. We have assumed that (1) we have adequately corrected for any spectral additions or interferences

from the host phase, (2) the presence or degree of hydration is not known, and (3) the mineral assemblage of any individual inclusion may be incomplete owing to accidental loss during opening. Nevertheless, SEM-EDS examination has provided valuable information regarding the composition and phase assemblages of the daughter minerals.

3.2.1. Daughter mineral analyses

The SEM-EDS analytical studies performed on the daughter crystals in FIs revealed the presence of the following minerals.

Chlorides. Na (halite) and K (sylvite) chlorides were identified in many opened inclusions (Fig. 8A,B). They were often associated and together occupied approximately 25% of the volume of the exposed portion of the inclusion. Both phases were cubic and some crystals had rounded edges. Fe- and Mn-chlorides commonly were identified and these often occurred as irregular masses or coated the wall of the inclusions.

Sulfides. Minerals showing Fe, Cu, and S EDS spectral peaks were identified as pyrite, (some were perhaps pyrrhotite), galena, and chalcopyrite, based on morphology and standardless EDS spectral analysis. These minerals often were found in association (Fig. 8D,E). We observed the uncommon occurrence of sphalerite and Ag_2S (argentite/acanthite). Monoclinic acanthite, the stable Ag_2S phase below 179°C, transforms to isometric argentite above 179°C. The habit of this phase was botryoidal and/or arborescent.

Sulfates. We identified the oxygen-bearing Ca and S phase as anhydrite ($CaSO_4$) based on apparent orthorhombic morphology (Fig. 8B,F).

Carbonates. Uncommon calcite was observed with no Mg noted above the SEM-EDS detection limit (~1000 ppm). Other carbonate phases are $ZnCO_3$ (smithsonite) (Fig. 8F) and a Pb-bearing phase (probable cerussite).

Tungsten and molybdenum-bearing phases. Uncommon scheelite (with a minor powellite component), identified on the basis of morphology and composition, occurs separately or in association with carbonate or sulfides (Fig. 8C).

Other minerals. Collected spectra frequently identified mixed Fe- and Mn-oxygen-bearing minerals which we identify as oxides or hydroxides. Apatite occurs as single, euhedral crystals, or in multiphase inclusions. A small Ca, Th, and REE phosphate was identified in one inclusion hosted by zircon. Two inclusions contain a very Mn-rich pyroxene (tentatively identified as johannsenite). We observed no major F-bearing phases in opened FIs.

3.2.2. Microthermometry

Since microthermometric data (Table 9) were collected on a limited number of samples and FI assemblages, results presented here should be considered preliminary but are nevertheless important to constrain the temperature and pressure of the nodule-forming environment.

FIs in potassium feldspar were found in healed fractures and are considered secondary; their dimensions seldom exceed 30 mm in length. The following types can be distinguished:

(1) one-phase inclusions ["Vapor only" (V), Type 1];
(2) three-phase inclusions [liquid + vapor + solid (Halite), Type 2].

In addition to FIs, we also identified several melt inclusions (MIs), partially or totally crystallized, which occur isolated or in small clusters, and are never related to any apparent

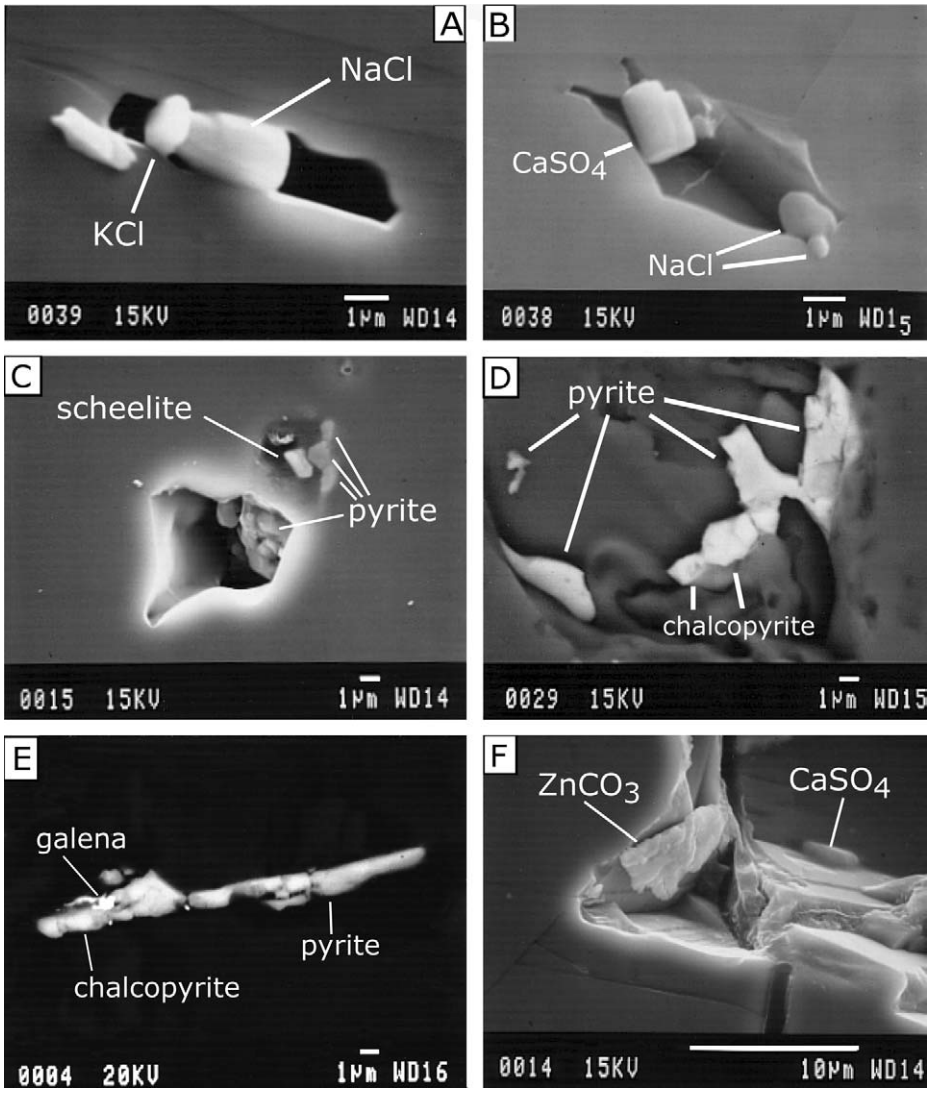

Figure 8. SEM images of opened fluid inclusions in host alkali feldspar. (A) Opened inclusion containing chlorides. NaCl (halite) and KCl (sylvite) chlorides are commonly found in opened inclusions in sample MT19 (secondary-electron SEM image). (B) $CaSO_4$ (anhydrite) and halite (NaCl) occurring in an opened fluid inclusion from sample MT19 (secondary-electron SEM image).(C) Opened fluid inclusion containing pyrite and scheelite from sample BL8 (secondary-electron SEM image). (D) SEM back-scattered image of a complex opened fluid inclusion which contains pyrite and chalcopyrite crystals. (E) Back-scattered SEM image of base-metal sulfides, galena, pyrite, and chalcopyrite along the edge of an opened inclusion from sample MT19. (F) SEM secondary-electron image of a complex opened inclusion containing a Zn carbonate and $CaSO_4$ (anhydrite) from sample BL8.

Table 9. Microthermometric data, Th, Tf, and NaCl (wt.% equivalent).

Th	Tf	NaCl (wt.%)
330	324	40.1
296	308	38.8
294	302	38.3
263	272	36.1
293	293	37.6
293	293	37.6
293	278	36.6
301	329	40.5
299	306	38.6
300	300	38.2
300	300	38.2
290	295	37.8
295	304	38.5
300	299	38.1
287	287	37.2
300	300	38.2
289	294	37.7
288	294	37.7
293	303	38.4
299	311	39.0
295	295	37.8
292	287	37.2
287	282	36.8
292	306	38.7
292	308	38.8
329	273	36.2
291	288	37.3
283	284	37.0
298	313	39.2
302	307	38.7
307	313	39.2
288	293	37.7
298	$\geq$ Th[a]	N/A
298	$\geq$ Th[a]	N/A
299	$\geq$ Th[a]	N/A
294	$\geq$ Th[a]	N/A
340	$\geq$ Th[a]	N/A

[a]In this case Tf is estimated to be slightly higher or equal to Th since poor visibility made detection of final halite melting impossible.

fracture or cleavage plane. They are thought to be primary. Tentative thermometric experiments (on a Linkam THS1500 heating stage calibrated in the temperature range of interest using the melting point of gold) found that the MIs start melting at ~950°C and are completely homogenized (i.e., total melting and complete bubble disappearance) at ~1150°C. This high temperature range may reflect previous loss of volatiles during cooling.

Type 1 FIs are closely associated with Type 2 and they appear either completely dark or "gray" with a thick rim (Fig. 9) in transmitted light. When heated or frozen they do not show any detectable phase change. We consider Type 1 FIs to be vapor-rich inclusions having a homogenization temperature (Th) $\leq$ 350°C. According to known phase relations, these inclusions would appear as single phase, vapor only, at room temperature (Bodnar et al., 1985).

Type 2 FIs contain a single daughter mineral of halite (Fig. 9A,B). Microthermometry gives homogenization temperatures [Th (L + V $\rightarrow$ L)] in the range 263–310°C, and temperatures of final disappearance (Tf) of the daughter mineral in the range 271–328°C (Table 9). Based on different homogenization behavior, Type 2 FIs can be further subdivided into:

Type 2a: Tf $>$ Th (in 49% of FIs halite disappears after the bubble);
Type 2b: Tf $<$ Th (in 20% of FIs halite disappears before the bubble);
Type 2c: Tf $\approx$ Th (in 31% of FIs halite and bubble disappear at the same time).

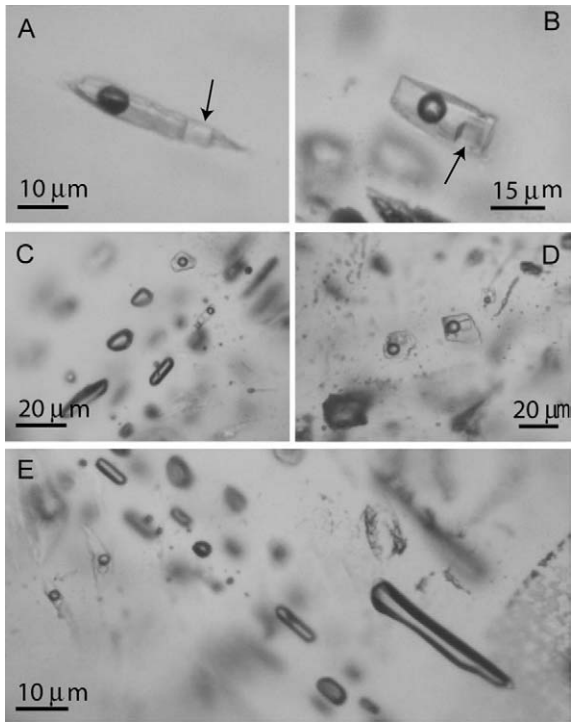

Figure 9. Transmitted light photomicrographs of fluid inclusions in BM nodules. (A, B) three-phase inclusions, the arrow indicates halide daughter crystals; (C, E) details of a plane of coexisting three-phase and vapor inclusions; (D) three-phase inclusions.

The coexistence of different homogenization behaviors with a relatively consistent salinity, independent from the homogenization mode, for halite-bearing FIs, is a well-known phenomenon reported in the porphyry copper literature (e.g., Bodnar and Beane, 1980).

Tf can be used to estimate salinity using the equation by Sterner et al. (1988; $\Psi = T°C/100$):

$$\text{Salinity (wt.\%)} = 26.242 + 0.4928\,\Psi + 1.42\,\Psi^2 - 0.223\,\Psi^3 + 0.04129\,\Psi^4 + 6.295 \times 10^{-3}\,\Psi^5 - 1.967 \times 10^{-3}\,\Psi^6 + 1.1112 \times 10^{-4}\,\Psi^7$$

This equation theoretically is valid only for FIs where Tf $\approx$ Th; however it can be used to approximate salinity where Tf $>$ Th, keeping in mind that the actual NaCl content will be over-or underestimated. The magnitude of the error will depend on both pressure in the inclusion at Tf and salinity. For our Tf range, and assuming that FIs internal pressure does not exceed 2 kbar (a reasonable assumption, considering that otherwise the inclusion would likely decrepitate), the error can be estimated at ± 1 wt.%. In this manner, the corresponding calculated salinity range for our FIs is 36–40 wt.% NaCl equivalent.

The coexistence of Type 1 and Type 2 FIs suggests that, at a certain point in the system evolution, boiling has occurred. However, it must be recognized that FIs that trapped a hypersaline fluid in the NaCl–H_2O system and that show homogenization behavior like Type 2a and 2c, cannot coexist with Type 1 owing to phase equilibrium constraints (Bodnar, 1994).

It is possible to explain the formation of these inclusions by calling upon two quite different scenarios:

Boiling did not occur (according to the phase equilibrium constraints in the NaCl-H_2O system; Bodnar, 1994). In this case, it is possible that high-salinity fluids were generated by direct exsolution from the magma during the late stages of crystallization. Type 2b inclusions would have been trapped at high P–T in field A (Fig. 10). Later, with the system cooling, P–T conditions would cross the isochore B where inclusions Type 2c could be trapped. Finally, further cooling would bring the system in the field C where Type 2a inclusions can be trapped. It is also possible to produce inclusions Type 2a, 2b, and 2c by significant pressure fluctuations at nearly constant T, though in this case the measured Th probably would have been spread over a wider range (Bodnar, 1992) than the range of our data (Fig. 11). Trapping temperatures for Type 2 inclusions can be tentatively inferred by relating the available data on pressures of formation of xenoliths at Mt. Somma-Vesuvius and Ventotene (1–3.5 kbar for Vesuvius, Belkin et al., 1985; Belkin and De Vivo, 1993; and 0.2–0.4 kbar for Ventotene, De Vivo et al., 1995) with the isochores obtained by the experimental data on the H_2O-NaCl system (Bodnar and Vityk, 1994). Calculations suggest that trapping temperatures are in the range 325–525°C.

Boiling did occur. In our case, the studied system is too complex to be adequately modeled by the phase relationships in the NaCl-H_2O system. This is compatible with the presence of varied and unusual hydrothermal mineral assemblages and also indicates that the fluids circulating in the system at the moment of the inclusion trapping were compositionally complex. Furthermore, the petrographic evidence of the coexistence of Type 1 and 2 inclusions is quite compelling. If we admit boiling, homogenization temperatures (Th) are to be considered as real trapping temperatures (Tt = 263–310°C), and trapping must have occurred under hydrostatic pressure at shallow depth.

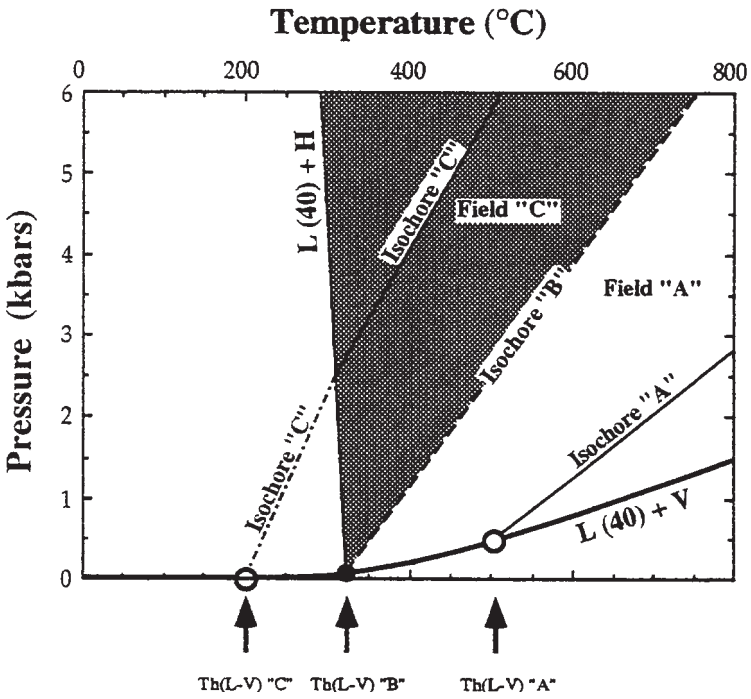

Figure 10. P–T diagram showing the three different modes of homogenization for a 40 wt.% NaCl FI (Bodnar and Vityk, 1994).

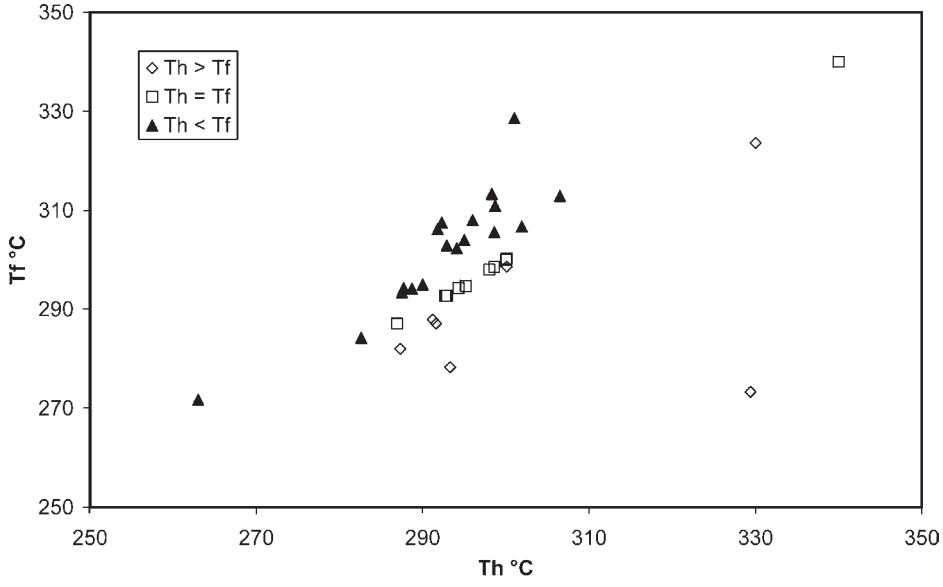

Figure 11. Th versus Tf for Fluid inclusions.

4. Discussion

4.1. Alkali-syenite nodules as samples of a magma chamber margin

Fundamental to our interpretation of the various textures, mineral phases, and microthermometry from the studied samples is that they are cognate with respect to the BM–CF magmatic system. All our evidence from chemistry, mineralogy, and petrography point to the fact that the studied samples are portions of an alkalic magma chamber margin that was broken up, entrained, and erupted with the BM deposits. Thus, features observed in these nodules allow us to tentatively describe the peripheral part of the magma chamber where the transition from a silicate liquid melt to a hypersaline aqueous fluid occurs.

The bulk of each nodule is potassium feldspar, precipitated from a trachytic magma and accumulated around the wall or bottom of the chamber. During pre-eruption crystallization, aqueous immiscible fluids may exsolve and become enriched in various incompatible elements. This may be especially important in the marginal region of the magma chamber where cooling and magma–wall rock interaction may be significant.

4.2. Textural development of the nodules

The mineral paragenesis and their petrographic relationships have recorded a transition from silicate melt-magmatic to hydrothermal aqueous fluid conditions. It is reasonable to assume that this transition was essentially isobaric with the major differences occurring in temperature and fluid composition. The particular unique volume that any nodule represents, would be progressively further away from the interface of magmatic melt/crystal accumulation as more and more crystals settled or migrated to the chamber margins. Figure 12 (A–C) illustrates this development whereby a loosely packed accumulation of early magmatic feldspar and mafic minerals becomes progressively mineralized, first with precipitation from a volatile-enriched silicate melt, followed by mineralization from exsolved, dense brines. Figure 13 shows a simplified paragenesis of the major mineral phases forming from the evolution of a magmatic (silicate melt) to a hydrothermal (aqueous brine) fluid. All high-temperature crystallization and/or alteration processes operating in the chamber margin would be quickly and effectively quenched during eruption. However, cooling of the erupted products may result in some further alteration.

This temperature transition from higher-temperature magmatic processes to lower-temperature aqueous processes has been documented during our study. Figure 14 shows the general pressure–temperature regime estimated for the studied nodules using measured temperature data and assumptions regarding pressure. In Figure 14, we have plotted mineral-pair geothermometers and the liquidus curve derived from the program MELTS (Ghiorso and Sack, 1993). For the two-feldspar geothermometer we used Nekvasil and Burnham (1987) from the program SOLVCALC, and for the hornblende–plagioclase geothermometer, we used Holland and Blundy (1994). Our assumption is that the mineral pairs were in equilibrium, which is supported by textural evidence. The recognition of equilibrium pairs is not a trivial matter, as pointed out by Mottana (1998). For any mineral pair (especially alkali feldspar and plagioclase) in these nodules, we observed overlapping petrogenetic stages in a single thin section.

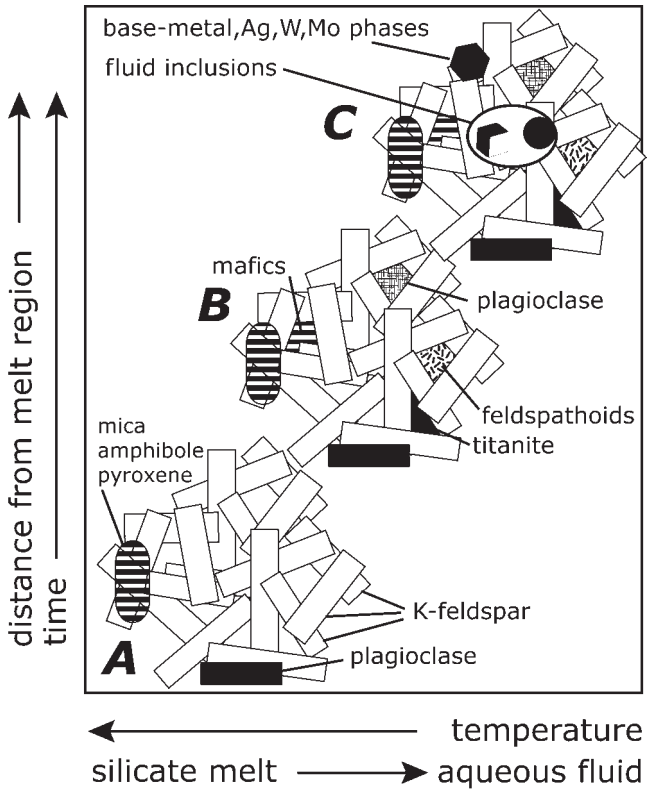

Figure 12. Schematic cartoon illustrating the mineralogical and textural evolution of the nodules, simplified into three main stages. The arrow-marked trends along the base and left side indicate, in general, the evolution of the average studied nodule. Each regime, A, B, and C, corresponds to the same small volume of magma chamber margin which was dislodged, entrained, and erupted with the BM products. (A) early magmatic accumulation of alkali feldspar, plagioclase, and mafics (mostly mica, amphibole, and clinopyroxene). This accumulation volumetrically was mostly K-feldspar and contained many vugs and "open" spaces. (B) The vugs and "open" spaces of the K-feldspar accumulation were filled with more mafics, Na-rich plagioclase, feldspathoids (scapolite and a cancrinite-group mineral), and phases rich in incompatible elements such as titanite, apatite, monazite, and Zr- and U-bearing minerals. (C) The last features we observe are the precipitation of chlorides, sulfates, base-metal, Ag, W, and Mo phases in fluid inclusions or in fractures.

Each nodule represents a small volume of chamber margin, which is different from any other nodule. The differences result from the particular location of the nodule volume and the differences that would be expected to occur around the margins of a crystallizing magma. Nevertheless, all the nodules display the same petrogenetic theme – early-formed magmatic-melt phases evolving to late-stage hypersaline brine precipitated phases.

4.3. Porphyry copper system analogue

The comparison between modern geothermal/hydrothermal systems and porphyry copper systems was studied to develop and enhance an exploration model (e.g., Burnham, 1979;

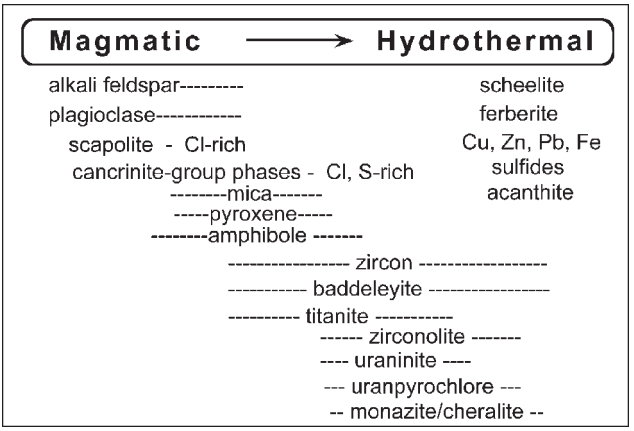

Figure 13. A simplified paragenetic scheme showing the main mineral phases as formed from a silicate-melt magmatic environment evolving to formation from a relatively high-temperature aqueous brine. We have used the general texture and observed mineralogical and fluid inclusion characteristics to classify the mineral phases. The general sequence of deposition is shown with more common phases at the top descending to less common ones toward the bottom. Phases such as ferberite, sulfides, and acanthite are late-stage but the details of their sequence of deposition are difficult to decipher as these phases are uncommon.

Beane, 1983). The research on active geothermal/hydrothermal systems was directed to understanding the processes, although the ultimate criterion for a "porphyry copper ore deposit" will be the mass of the metal deposited. Sasada (2000) discusses the geothermal porphyry copper analogue and concludes that the major alteration difference, at least in the context of Japanese geothermal systems, is that porphyry copper systems have a pervasive potassium-rich alteration. The BM–CF system is developed in an high-potassium magmatic environment. Further evolution of the hydrothermal system may lead to potassic alteration. The Burnham (1979) model, whereby crystallizing magmas become progressively enriched in volatiles and exsolve an aqueous fluid rich in incompatible elements, such as Cl, REE, metals, etc., is compatible with our mineralogical, textural, and chemical observations of the nodules.

De Vivo and Lima (this volume) have addressed the problem of frequent ground movements (bradyseisms) in the CF volcanic region. They suggest that hydrothermal processes driven by heat evolved from the cooling magma at depth are responsible for the ground movements.

4.4. Magmatic–hydrothermal transition

In the alkali-syenite nodules of the BM we found textural, mineralogical, and chemical evidence that suggests they recorded a transition from magmatic to hydrothermal conditions. The nodules primarily are composed of alkali feldspars (up to 80%) with subordinate plagioclase, scapolite, a S- and Cl-rich member of the cancrinite group, amphibole, clinopyroxene, biotite, titanomagnetite, titanite, and apatite.

SEM-EDS and electron microprobe analyses of the nodules provide evidence for the presence of U, Zr, Nb, Th, and REE elements in late-stage minerals such as apatite, Zr-bearing minerals (i.e., zircon and baddeleyite), pyrochlore-group minerals, thorite, and

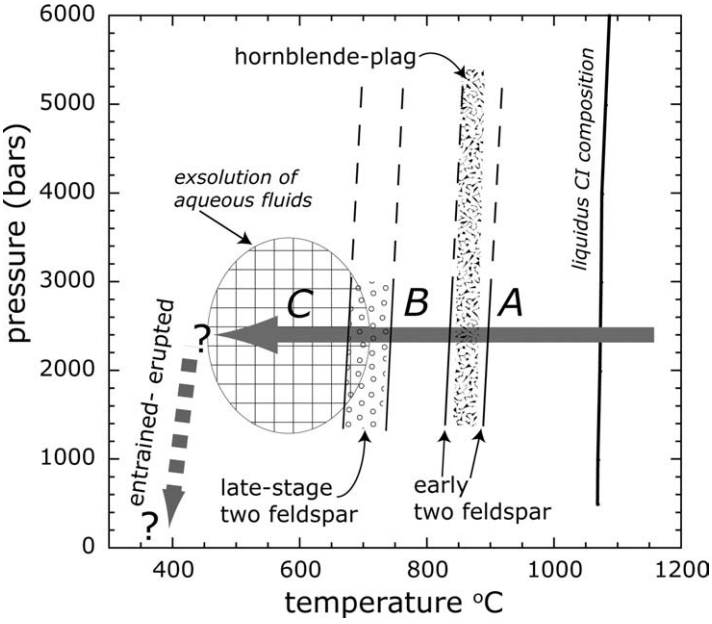

Figure 14. A schematic cartoon in pressure/temperature space that illustrates the evolution of the studied nodules. Here we have used various mineral-pair geothermometers, fluid inclusion data, and liquidus temperatures to construct a reasonable PT evolution of the nodules. The liquidus curve is derived from MELTS (Ghiorso and Sack, 1993) using the average CI whole-rock composition given in Table 2. The general range of the temperatures from early-alkali feldspar–plagioclase pairs is shown by two curves and the field (small open circles) is shown for texturally late-stage alkali feldspar–plagioclase pairs (both using Nekvasil and Burnham, 1987). The temperature is extrapolated to higher pressures by the dashed lines. The field for the hornblende–plagioclase geothermometer data (Holland and Blundy, 1994) is shown by a pattern. The general, estimated PT field for the exsolution of aqueous fluid is shown. The horizontal arrow traces, in general, the PT evolution of the average nodule from the melt environment to the PT time just before entrainment and eruption. We have chosen a constant pressure of about 2200 bars, corresponding to a depth of 8 km (assuming an overburden density of 2.7 g/cm^3). With regard to the liquidus and mineral-pair geothermometer data, their curves are very steep so the exact pressure regime assumption is not critical. The letters, A, B, and C mark the general PT areas as outlined by Figure 12.

phosphate (monazite group). Many of these accessory minerals occur with typical hydrothermal textures (i.e., as replacement, in vugs or as infillings). Microprobe data show the partition of fluorine, chlorine, and sulfur in the syenite nodules. Fluorine is incorporated in biotite and subordinately in amphibole, while chlorine and sulfur are incorporated in scapolite, cancrinite-group minerals and trapped in as FIs. Complex assemblages of daughter minerals found in multiphase FIs in the nodules of the BM are evidence of the trapping of high-solute fluids. Abundance of chlorides, sulfides, and to a lesser extent sulfates and carbonates, suggest that FIs trapped a hypersaline/sulfur-rich fluid (possibly with minor CO_2), which might have been exsolving from a crystallizing magma.

Preliminary microthermometry and observations on secondary hypersaline FIs in K-feldspars suggest two possible scenarios for fluid trapping: (1) circulation of non-boiling, high-temperature (up to 525°C), high-salinity fluids which possibly were trapped under

decreasing P–T conditions; and (2) circulation of boiling, hypersaline fluids, trapped at low pressure and temperatures up to 300°C.

The strong petrographic evidence for the coexistence of Type 1 (vapor) and Type 2 (hypersaline) FIs, seems to suggest that, at least, these particular inclusions are trapped boiling fluids and formed in a later hydrothermal stage.

In the last decade, many studies of magma chamber margins in alkali-enriched magmatic systems (Turbeville, 1992; Federico et al., 1994; Belkin et al., 1994, 1996; Renzulli et al., 1995; Fulignati et al., 1997; Tarzia et al., 1999, 2000; Gilg et al., 2001) demonstrated that these peripheral areas can show selective enrichment of incompatible elements (i.e., U, Th, Zr, REE) with features similar to those found in the BM nodules.

4.5. Nature of the exsolved aqueous fluid

Many studies on magmatic systems (Roedder, 1984 and references therein) report the presence of high-salinity FIs (i.e., the presence of a Cl-rich, high-density aqueous phase). Similar occurrences are also reported from Italian subvolcanic systems (De Vivo et al., 1992, 1993, 1995; Lowenstern, 1994; Belkin et al., 1996).

Experimental studies have pointed out that many metals tend to partition into a hypersaline chloride-bearing brine exsolved from a silicate melt (Candela, 1986, 1989; Cline and Bodnar, 1991; Shinohara, 1994; Candela and Piccoli, 1995; Kamenetsky et al., 2003). Similarly, trace and REE elements can be efficiently extracted from magma by Cl-rich fluids (Kravchuk and Keppler, 1994; Haas et al., 1995). Sulfate-rich fluids are reported in peralkaline silicic magmatic intrusions and in orthomagmatic fluids related to porphyry copper deposits (Roedder, 1984). Furthermore, under oxidizing conditions, S fugacity constraints yield a sulfur-rich vapor exsolving from a crystallizing magma (Carroll and Rutherford, 1985).

The occurrence of sulfides together with chlorides, sulfates, and Fe-, Mn-oxides in the nodules and as daughter minerals suggest that the redox state of the nodule-forming environment shifted progressively toward more oxidized conditions. Concerning the partition of REE into S-rich fluid, Wood (1990) states that sulfate–REE complexes can predominate over aqueous species in the absence of other ligands. Furthermore, temperature strongly affects the REE-complex stability constant: increasing temperatures produce an increase in the stability constant values for fluoride, sulfate, and chloride (in that order). Therefore, chloride and sulfates, which were present in the peripheral magma chamber system of the BM magma, could have played an important role in the selective enrichment of REE in the accessory minerals of the nodules.

4.6. W (Mo) enrichment

The detailed nodule petrography and mineralogy revealed many occurrences of W (Mo) mineral species (scheelite–powellite, ferberite). Although these nodules are not exceptionally mineralized in comparison to typical W-skarn deposit samples, they do contain an interesting assemblage of W (Mo) mineral species. Manning and Henderson (1984) demonstrated that chloride complexes can efficiently extract tungsten from magmatic melts into an aqueous phase. This suggests that an exsolving aqueous phase most likely

extracted W and Mo from the magma and transported these elements to the nodule environment where cooler conditions or some particular reaction caused precipitation.

5. Concluding remarks

The alkali-syenite nodules found in the BM deposit display convincing evidence of a transition from a magma-dominated system to a fluid-dominated hydrothermal system. This transition took place along the margins of a magma chamber where a magma of trachytic composition was sufficiently evolved to exsolve an aqueous fluid carrying a complex solute, containing high amounts of incompatible elements. Textures, mineralogy, and mineral chemistry of the nodules and nature of FI of daughter minerals all point toward this interpretation. The various sulfides and tungstates observed in the nodules suggest the potential for an ore deposit somewhere (or sometime) in this volcanic system.

Acknowledgements

The authors wish to thank Carter Hearn (Smithsonian, USGS retired) and Paul C. Hackley (USGS) for their constructive reviews. The work benefited from partial funds from GNV-INGV to B. De Vivo (2003).

References

Ballirano, P., Maras, A., Buseck, P.R., 1996. Crystal chemistry and IR spectroscopy of Cl- and SO_4-bearing cancrinite-like minerals. Am. Mineral. 81, 1003–1012.

Beane, R.E., 1983. The magmatic–meteoric transition. Geotherm. Res. Counc. Spec. Rep. 13, 245–253.

Belkin, H.E., Cavarretta, G., Tecce, F., 1994. Petrogenesis of leucite-bearing nodules from Colli Albani Volcano ejecta, Latium, Italy. Abstracts International Mineralogical Association, 16th General Meeting, 4–9 September, Pisa, Italy, p. 35.

Belkin, H.E., De Vivo, B., 1993. Fluid inclusion studies of ejected nodules from plinian eruptions of Mt. Somma-Vesuvius. J. Volcanol. Geotherm. Res. 58, 89–100.

Belkin, H.E., De Vivo, B., Lima, A., Török, K., 1996. Magmatic silicate/saline/sulfur rich/CO_2 immiscibility and zirconium and REE enrichment from alkaline magma chamber margins: evidence from Ponza Island and Pontine archipelago, Italy. Eur. J. Mineral. 8, 1401–1420.

Belkin, H.E., De Vivo, B., Roedder, E., Cortini, M., 1985. Fluid inclusion geobarometry from ejected Mt. Somma-Vesuvius nodules. Am. Mineral. 70, 288–303.

Bellucci, F., Milia, A., Rolandi, G., Torrente, M.M., this volume. Structural control on the Upper Pleistocene ignimbrite eruptions in the Neapolitan area (Italy): volcano tectonic faults versus caldera faults.

Bodnar, R.J., 1992. Can we recognize magmatic fluid inclusions in fossil systems based on room temperature phase relations and microthermometric behavior? Geol. Surv. Jpn. Rep. 279, 26–30.

Bodnar, R.J., 1994. Synthetic fluid inclusions: XII. The system H_2O-NaCl. Experimental determination of the halite liquidus and isochores for a 40 wt.% NaCl solution. Geochim. Cosmochim. Acta 58, 1053–1063.

Bodnar, R.J., Beane, R.E., 1980. Temporal and spatial variations in hydrothermal fluid characteristics during vein filling in preore cover overlying deeply buried porphyry copper-type mineralization at Red Mountain, Arizona. Econ. Geol. 75, 876–893.

Bodnar, R.J., Burnham, C.W., Sterner, S.M., 1985. Synthetic fluid inclusions in natural quartz. III. Determination of phase equilibrium properties in the system H_2O-NaCl to 1000°C and 1500 bars. Geochim. Cosmochim. Acta 49, 1861–1873.

Bodnar, R.J., Vityk, M.O., 1994. Interpretation of microthermometric data for H_2O-NaCl fluid inclusions. 117-130. In: De Vivo, B., Frezzotti, M.L. (Eds), Fluid Inclusions in Minerals: Methods and Applications. Short Course of the Working Group (IMA) "Inclusions in minerals", Pontignano, Siena, 1–4 September, 376pp.

Borodin, L.S., Bykova, A.B., Kapitanova, T.A., Pyatenko, Y.U.A., 1960. New data on zirconolite and its niobium variety. Dokl. Acad. Sci, Earth Sci. Sec. 134, 1022–1024.

Branney, M.J., Kokelaar, B.P., 1992. A reappraisal of ignimbrite emplacement: progressive aggradation and particulate to non-particulate flow transition during emplacement of high-grade ignimbrite. Bull. Volcanol. 54, 504–520.

Brøgger, W.C., 1890. Die Mineralien der Syenitpegmatitgänge der Südnorwegischen Augit- und Nephelinsyenite. 46. Polymignyt. Z. Krystall. Mineral. 16, 387–396.

Burnham, C.W., 1979. Magmas and hydrothermal fluids. In: Barnes, H.L. (Ed.), Geochemistry of Hydrothermal Ore Deposits. Wiley, New York, pp. 71–136.

Candela, P.A., 1986. Towards a thermodynamic model for the halogens in magmatic systems; an application to melt-vapor-apatite equilibria. Chem. Geol. 57, 289–301.

Candela, P.A., 1989. Calculation of magmatic fluid contributions to porphyry-type ore systems: predicting fluid inclusion chemistries. Geochem. J. 23, 295–305.

Candela, P.A., Piccoli, P.M., 1995. Model oremetal partitioning from melts into vapor and vapor/brine mixtures. MAC Short Course Ser. 23, 101–127.

Caprarelli, G., Tsutsumi, M., Turi, B., 1997. Chemical and signatures of the basement rocks from the Campi Flegrei geothermal field (Naples, southern Italy): inferences about the origin and evolution of its hydrothermal fluids. J. Volcanol. Geotherm. Res. 76, 63–82.

Carroll, M.R., Rutherford, M.J., 1985. Sulfide and sulfate saturation in hydrous silicate melts. J. Geophys. Res. 90, C601–C612.

Cline, J.S., Bodnar, R.J., 1991. Can economic porphyry copper mineralization be generated by a typical calcalkaline melt? J. Geophys. Res. 96, 8113–8126.

Cline, J.S., Bodnar, R.J., 1994. Direct evolution of brine from crystallizing silicic melt at Questa, New Mexico, molybdenum deposit. Econ. Geol. 89, 1780–1802.

Deer, W.A., Howie, R.A., Wise, W.S., Zussman, J., 2004. Rock-Forming Minerals, Volume 4B: Framework Silicates, Silica minerals, Feldspathoids, and the Zeolites. The Geological Society, London, 982pp.

De Vivo, B., 1999. Fluids in volcanic and plutonic environments: evidence from fluid inclusions. In: Marshall, C.P., Fairbridge, E.W. (Eds), Encyclopedia of Geochemistry. Kluwer Academic Publishers, Dordrecht, NL, pp. 250–252.

De Vivo, B., Belkin, H.E., Barbieri, M., Chelini, W., Lattanzi, P., Lima, A., Tolomeo, L., 1989. The Campi Flegrei (Italy) geothermal system: a fluid inclusion study of the Mofete and san Vito fields. J. Volcanol. Geotherm. Res. 36, 303–326.

De Vivo, B., Frezzotti, M.L., Lima, A., 1993. Immiscibility in magmatic differentiation and fluid evolution in granitoid xenoliths at Pantelleria: fluid inclusion evidence. Acta Vulcanol. 3, 195–202.

De Vivo, B., Frezzotti, M.L., Mahood, G., 1992. Fluid inclusions in xenoliths yield evidence for fluid evolution in peralkaline granitic bodies at Pantelleria (Italy). J. Volcanol. Geotherm. Res. 52, 295–301.

De Vivo, B., Lima, A., this volume. An hydrothermal model to explain the ground movements (bradyseism) at Campi Flegrei.

De Vivo, B., Rolandi, G., Gans, P.B., Calvert, A., Bohrson, W.A., Spera, F.J., Belkin, H.E., 2001. New constraints on the eruptive history of the Campanian volcanic plain (Italy). Mineral. Petrol. 73, 47–65.

De Vivo, B., Török, K., Ayuso, R.A., Lima, A., Lirer, L., 1995. Fluid inclusion evidence for magmatic silicate/saline/CO_2 immiscibility and geochemistry of alkaline xenoliths from Ventotene island (Italy). Geochim. Cosmochim. Acta 59, 2941–2953.

Di Girolamo, P., Ghiara, M.R., Lirer, L., Munno, R., Rolandi, G., Stanzione, D., 1984. Vulcanologia and petrologia dei Campi Flegrei. Boll. Soc. Geol. It. 103, 349–413.

Droop, G.T.R., 1987. A general equation for estimating Fe^{3+} concentrations in ferromagnesian silicates and oxides from microprobe analyses, using stoichiometric criteria. Mineral. Mag. 51, 431–435.

Federico, M., Peccerillo, A., Barbieri, A., Wu, T.W., 1994. Mineralogical and geochemical study of granular xenoliths from the Alban Hill, Central Italy: bearing on evolutionary processes in potassic magma chambers. Contrib. Mineral. Petrol. 115, 384–401.

Fisher, R.V., Orsi, G., Ort, M., Heiken, G., 1993. Mobility of large volume pyroclastic flow – emplacement of the Campanian Ignimbrite, Italy. J. Volcanol. Geotherm. Res. 56, 205–220.

Fowler, M.B., Williams, C.T., 1986. Zirconolite from the Glen Dessarry syenite: a comparison with other Scottish zirconolites. Mineral. Mag. 50, 326–328.

Fulignati, P., Gioncada, A., Maineri, C., Sbrana, A., 1997. A first insight into the magmatic–hydrothermal system related to 79 AD eruption magmatic chamber of Vesuvius (Italy). XIV ECROFI, Nancy, Abstract, 115–116.

Ghiorso, M.S., Sack, R.O., 1993. MELTS; software for the thermodynamic analysis of phase equilibria in magmatic systems. Geol. Soc. Am. Abstr. Pr. 25, 96.

Gianfagna, A., 1985. Occurrence of baddeleyite – ZrO_2 – in an ejected block from Colle Cimino, Marino (Alban Hills, Italy). Periodico di Mineralogia 54, 129–133.

Gieré, R., Williams, C.T., Lumpkin, G.R., 1998. Chemical characteristics of natural zirconolite. Schweiz. Mineral. Petrogr. Mitt. 78, 433–459.

Gilg, H.A., Lima, A., Somma, R., Belkin, H.E., De Vivo, B., Ayuso, R.A., 2001. Isotope geochemistry and fluid inclusion study of skarns from Vesuvius. Mineral. Petrol. 73, 145–176.

Haas, J.R., Shock, E.L., Sassani, D.A., 1995. Rare earth elements in hydrothermal systems: estimates of standard partial molal thermodynamic properties of aqueous complexes of the rare earth elements at high pressures and temperatures. Geochim. Cosmochim. Acta 59(21), 4329–4350.

Holland, T., and Blundy, J., 1994. Non-ideal interactions in calcic amphiboles and their bearing on amphibole-plagioclase thermometry. Contrib. Mineral. Petrol. 116(4), 433–447.

Johnston-Lavis, H.J., 1889. Report of the committee appointed for the investigation of the volcanic phenomena of Vesuvius and its neighbor. The Royal Society, London.

Kamenetsky, V.S., Wolfe, R.C., Eggins, S.M., Mernagh, T.P., Bastrakov, E., 1999. Volatile exsolution at the Dinkidi Cu–Au porphyry deposit, Philippines: a melt-inclusion record of the initial ore-forming process. Geology 27, 691–694.

Kamenetsky, V.S., De Vivo, B., Naumov, V.B., Kamenetsky, M.B., Mernagh, T.P., Van Achterbegh, E., Ryan, C.G., Davidson, P., 2003. Magmatic inclusions in the search for natural silicate-salt melt immiscibility: methodology and examples. In: De Vivo, B., Bodnar, R.J. (Eds), Melt Inclusions in Volcanic Systems. Methods, Applications and Problems. Series: Developments in Volcanology, Vol. 5, Elsevier, Amsterdam, pp. 65–82.

Kelley, K.D., Romberger, S.D., Beaty, D.W., Pontius, J.A., Snee, L.W., Stein, H.J., Thompson, T.B., 1998. Geochemical and geochronological constraints on the genesis of Au-Te deposits at Cripple Creek, Colorado. Econ. Geol. 93, 981–1012.

Kilinc, I.A., Burnham, C.W., 1972. Partitioning of chloride between a silicate melt and coexisting aqueous phase from 2 to 8 kilobars. Econ. Geol. 67, 231–235.

Kravchuk, I.F., Keppler, H., 1994. Distribution of chloride between aqueous fluid and felsic melts at 2 kbars and 800°C. Eur. J. Mineral. 6, 913–923.

Larsen, A.O., 1996. Rare earth minerals from the syenite pegmatites in the Oslo region, Norway. In: Jones, A.P., Wall, F., Williams, C.T. (Eds), Rare Earth Minerals: Chemistry, Origin and Ore Deposits. Mineralogical Society Series 7. Chapman and Hall, London, UK, pp. 151–166.

Le Maitre, R.W. (Ed.), 2002. Igneous Rocks, A Classification and Glossary of Terms, 2nd ed. Cambridge University Press, Cambridge, p. 236.

Lirer, L., Perrotta, A., Rolandi, G., Rubin, M., Donahue, D., 1991. The Campi Flegrei "Museum Breccia" deposits: eruptive events younger than Campanian Ignimbrite Formation. International Conference on Active Volcanic Risk Mitigation, Abstracts.

Lowenstern, J.B., 1994. Chlorine, fluid immiscibility, and degassing in peralkaline magmas from Pantelleria, Italy. Am. Mineral. 79, 353–369.

Lowenstern, J.B., Persing, H.M., Wooden, J.L., Lanphere, M., Donnelly-Nolan, J., Grove, T.L., 2000. U–Th dating of single zircons from young granitoid xenoliths: new tools for understanding volcanic processes. EPSL 183, 291–302.

Manning, D.A.C., Henderson, P., 1984. The behavior of tungsten in granitic melt vapor system. Contrib. Mineral. Petrol. 86, 286–293.

Mazzi, F., Munno, R., 1983. Calciobetafite (new mineral from the pyrochlore group) and related minerals from Campi Flegrei, Italy: crystal structures of polymignyte and zirkelite: comparison with pyrochlore and zirconolite. Am. Mineral. 68, 262–276.

Melluso, L., Morra, V., Perrotta, A., Scarpati, C., Adabbo, M., 1995. The eruption of the Breccia Museo (Campi Flegrei, Italy): fractional crystallization processes in a shallow, zoned magma chamber and implications for the eruptive dynamics. J. Volcanol. Geotherm. Res. 68, 325–339.

Mottana, A., 1998. Sanidine holocrystalline ejecta from central Sabatini Volcanic District, Latium (Italy), II Intergranular ejecta and minerogenetic deductions. Rend. Fis. Acc. Lincei. 9, 131–143.

Nekvasil, H., Burnham, C.W., 1987. The calculated individual effects of pressure and water content on phase equilibria in the granite system. In: Mysen, B.D. (Ed), Magmatic Processes, Physicochemical Principles; A Volume in Honor of Hatten S. Yoder, Jr., Special Publication – The Geochemical Society, Vol. 1, pp. 433–445.

Orsi, G., de Vita, S., Di Vito, M., 1996. The restless, resurgent Campi Flegrei nested caldera (Italy): constraints on its evolution and configuration. J. Volcanol. Geotherm. Res. 74, 179–214.

Paone, A., 1999. Modellizzazione dei processi metallogenetici associati a vulcanismo di tipo alcalino. Potenziale della provincia vulcanica Napoletana. Ph.D. thesis, Università degli studi di Napoli "Federico II".

Paone, A., Ayuso, R.A., De Vivo, B., 2001. A metallogenic survey of alkalic rocks of Mt. Somma-Vesuvius volcano. Mineral. Petrol. 73, 201–233.

Perrotta, A., 1992. Evoluzione vulcanologica dei Campi Flegrei tra 20,000 and 12,000 anni and dinamica dell'eruzione della Breccia Museo. Ph.D. thesis, Università di Napoli, 103pp.

Perrotta, A., Scarpati, C., 1994. The dynamics of the Breccia Museo eruption (Campi Flegrei. Italy) and the significance of spatter clasts associated with lithic breccias. J. Volcanol. Geotherm. Res. 59, 335–355.

Renzulli, A., Upton, B.G.J., Nappi, G., 1995. Magma chamber processes preceding the Pitigliano Formation eruption (Latera volcanic complex, central Italy): evidence from cognate plutonic clasts. Acta Vulcanol. 7, 55–74.

Roedder, E., 1971. Fluid inclusion studies on the porphyry-type ore deposits at Bingham, Utah, Bute, Montana and Climax, Colorado. Econ. Geol. 66, 98–120.

Roedder, E., 1984. Fluid inclusions. Reviews in Mineralogy, Vol. 12. Min. Soc. Am., 644pp.

Rolandi, G., Bellucci, F., Heisler, M.T., Belkin, H.E., De Vivo, B., 2003. Tectonic controls on the genesis of ignimbrites from the Campanian Volcanic Zone, Southern Italy. Mineral. Petrol. 79, 3–31.

Rosi, M., Sbrana, A., 1987. Phlegrean Fields. CNR, Quaderni della Ricerca Scientifica, 114(9), 175pp.

Rosi, M., Sbrana, A., Principe, C., 1983. The Phlegrean Fields: structural evolution, volcanic history and eruptive mechanisms. J. Volcanol. Geotherm. Res. 17, 273–288.

Rosi, M., Vezzoli, L., 1989. I depositi prossimali di breccia associati all'eruzione dell'Ignimbrite Campana (Campi Flegrei). Boll. GNV 979–998.

Rosi, M., Vezzoli, L., Aleoti, P., De Censi, M., 1991. Campanian Ignimbrite eruption: proximal deposits. CEV Field Guide, pp. 41–74.

Sasada, M., 2000. Igneous-related active geothermal system versus porphyry copper hydrothermal system. Proceedings World Geothermal Congress 2000, Kyushu-Tohoku, Japan, 1691–1693.

Shinohara, H., 1994. Exsolution of immiscible vapor and liquid phases from a crystallizing silicate melt: implications for chlorine and metal transport. Geochim. Cosmochim. Acta 58, 5215–5221.

Sterner, S.M., Hall, D.L., Bodnar, R.J., 1988. Synthetic fluid inclusions. V. Solubility relations in the system NaCl-KCl-H_2O under vapor-saturated conditions. Geochim. Cosmochim. Acta 52, 989–1005.

Tarzia, M., De Vivo, B., Belkin, H.E., 2000. Occurrence of uranium, zirconium and REE bearing minerals in alkali syenite nodules from the Breccia Museo pyroclastic deposit, Naples, Italy. EOS 81(48), 1272.

Tarzia, M., Lima, A., De Vivo, B., Belkin, H.E., 1999. Uranium, zirconium and rare earth element enrichment in alkali syenite nodules from the Breccia Museo Deposit, Naples, Italy. Geol. Soc. Am. Abst. Pr. 31(7), A-69.

Turbeville, B.N., 1992. Relationship between chamber margin accumulates and pore liquids: evidence from arrested in situ processes in ejecta, Latera caldera, Italy. Contrib. Mineral. Petrol. 100, 429–441.

Wen, S., Nekvasil, H., 1994. SOLVCALC; an interactive graphics program package for calculating the ternary feldspar solvus and for two-feldspar geothermometry. Comput. Geosci. 20, 1025–1040.

Williams, C.T., Gieré, R., 1996. Zirconolite: a review of localities worldwide, and a compilation of its chemical composition. Nat. Hist. Mus. London Bull. 52, 1–24.

Wood, S.A., 1990. The aqueous geochemistry of the rare earth elements and yttrium 2. Theoretical predictions of speciation in hydrothermal solutions to 350°C at saturation water vapor pressure. Chem. Geol. 88, 99–125.